Wave Transmission and Force on Nearshore Rapidly-Installed Breakwater

by

Hiroaki Hosoi, Nobuhisa Kobayashi and Jeffrey A. Melby

RESEARCH REPORT NO. CACR-03-01
March, 2003

Center for Applied Coastal Research
Ocean Engineering Laboratory
University of Delaware
Newark, DE 19716

ABSTRACT

A numerical model based on finite-amplitude, shallow-water wave theory is developed to predict irregular wave breaking and transmission as well as wave force on an innovative Shore-RIB structure that consists of one or two tubes held by an anchored fabric shroud. The numerical model slightly underpredicts the measured transmission coefficient which decreased linearly with the increase of the ratio between the crest elevation of the structure and the incident spectral significant wave height. The predicted maximum fabric tension predicted using the computed maximum horizontal wave force is in fair agreement with the measured tension. The difficulties in predicting the temporal variations of the fabric tension due to intermittent tube oscillations are discussed using the measured and predicted time series and spectra of the fabric tension. For practical applications, it is recommended to minimize the temporal range of the fabric tension between the static fabric pre-tension and the predicted maximum fabric tension.

ACKNOWLEDGEMENTS

This study was supported partly by the U.S. Army Corps of Engineers, Coastal and Hydraulics Laboratory under Contract No. DACA42-02-P-0041.

This report is essentially the same as the thesis written by the first author, Hiroaki Hosoi, for the Master's degree of the Department of Civil Engineering, Nagoya University in Nagoya, Japan. The first author would like to thank Professors Koichiro Iwata, Norimi Mizutani and Hiroshi Tagawa for their valuable comments and encouragement to complete this thesis as the continuation of his research at the Center for Applied Coastal Research, University of Delaware, during April, 2001 to March, 2002.

Contents

1 INTRODUCTION

In many coastal countries the economic activities and population are concentrated along the coastline. The utilization and development of the coastal regions are likely to increase in the future. As a result, it is essential to maintain and improve port and harbor facilities and to develop mitigation measures against coastal hazards caused by storms and tsunamis. At the same time, coastal utilization and development will need to be sustainable and in harmony with the coastal environment. Coastal structures will remain essential for future coastal utilization and development as reviewed by Kobayashi (1999).

Breakwaters with low crests have been constructed for shoreline stabilization and harbor protection. The low crest reduces construction cost but increases wave transmission. The wave transmission coefficient defined as the ratio between the incident and transmitted wave heights depends on the incident wave characteristics, the crest height and width, and the structure slope, roughness and permeability on the basis of available empirical formulas (D'Angremond et al. 1996; Seabrook and Hall 1998). The most important parameter for the empirical estimation of the wave transmission coefficient is the ratio between the crest height above the still water level and the incident design wave height such as the significant wave height. On the other hand, Kobayashi and Wurjanto (1989) developed a time-dependent numerical model to examine the wave dynamics involved in wave reflection, breaking and transmission over a submerged breakwater. Their numerical model was shown to be in good agreement with a set of laboratory data on regular wave reflection and transmission coefficients.

On the other hand, softer, flexible or floating structures have also been constructed to reduce the construction cost in comparison to the solid structures fixed on the seabed. Ohyama et al. (1989) proposed a flexible mound consisting of a horizontal membrane bag filled with water and attached to the seabed. They developed a linear wave model to study the wave transmission and reflection characteristics of the flexible mound and compared their model with experimental data. Phadke and Cheung (1999) improved their linear wave model by analyzing the membrane more realistically. Other membrane structures attached on the seabed were examined by Broderick and Leonard (1995), Liapis et al. (1996) and Devi et al. (1999). Milgram et al. (1971) examined the structural and hydrodynamic forces on a flexible, floating barrier used as a containment device for floating liquid pollutants such as oil. Sawaragi et al. (1989) calculated wave reflection and transmission by a submerged vertical membrane lifted by floats. Cho et al (1997) investigated the performance of flexible-membrane wave barriers, whereas Ohyama et al. (2000) computed the floating-body motion in nonlinear random waves.

Van der Meer et al. (2000) conducted laboratory experiments and analyzed the spectral changes between incident and transmitted waves. Kobayashi and Wurjanto (1992) developed a numerical model to investigate irregular wave setup and runup on beaches. Kobayashi and Raichle (1994) applied this numerical model to predict irregular wave overtopping of revetments in the surf zone.

The U.S. Army Corps of Engineers, Coastal and Hydraulics Laboratory has been developing a nearshore rapidly-installed breakwater (Shore-RIB) to protect and facilitate landing operations for nearshore logistics over the shore as illustrated in Fig. 1.1. One of the Shore-RIB concepts tested in a wave flume by Melby and Resio (2002) consisted of water-filled high-tenacity high-strength fabric tubes held by an anchored fabric shroud. Since only fabric shroud and tubes are required, the construction cost of this structure is much less than a conventional type of breakwater. In addition, the Shore-RIB can be removed and redeployed at another site. Consequently, civilian applications of the Shore-RIB are promising at sites of moderate wave action. Melby and Resio (2002) measured the wave forces on the fabric shroud covering the tubes and the irregular wave transmission coefficient for ranges of incident wave conditions, structure freeboards, structure configurations, and shroud pre-tension. In designing such

breakwaters, it is essential to predict the wave reflection and transmission coefficients, wave forces, and structure response. A numerical model is developed here to predict the irregular wave breaking and transmission and the wave force on the submerged and emerged Shore-RIB structures. The numerical model is verified using the laboratory measurements by Melby and Resio (2002). The verified numerical model is used to examine the cross-shore and temporal variations of the free surface, horizontal velocity and pressure on the structure which were not measured in the experiments. The numerical model and the quantitative understanding gained from the predicted wave dynamics can be used to optimize the Shore-RIB configuration because it is easier to change the structure geometry and examine the corresponding wave dynamics in the numerical model.

In the following, the experiments and measurements of the wave transmission coefficient and fabric tension performed by Melby and Resio (2002) are summarized in Chapter 2 because their experimental results are essential in this study but are not available easily. In Chapter 3, the numerical model developed in this study is presented in detail. In Chapter 4, the computed results including the reflection coefficient, transmission coefficient, free surface profile and horizontal velocity variation, time-averaged wave energy balance and wave forces on the Shore-RIB are presented and discussed. In Chapter 5, comparison is made between the measured and computed wave transmission coefficients. In addition, the maximum fabric tension measured for each test is predicted using the maximum horizontal wave force predicted by the numerical model. Finally, Chapter 6 presents the summary and conclusion of this study.

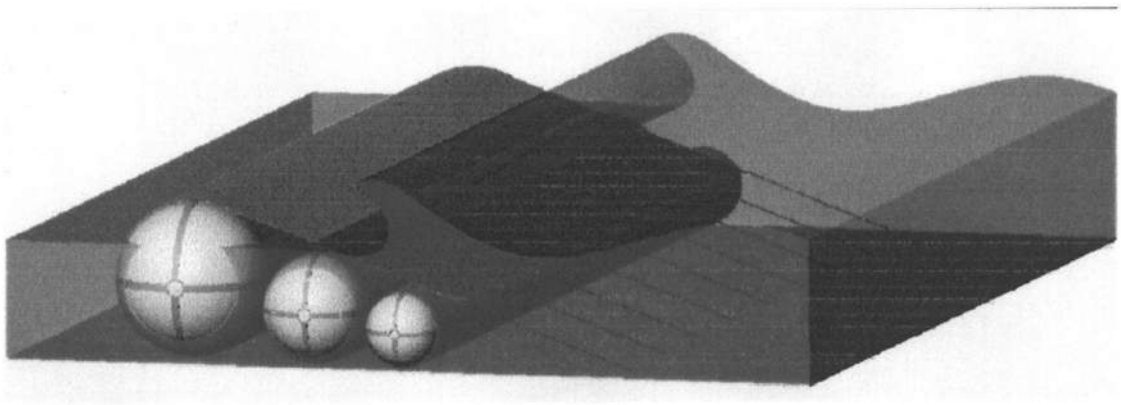

Fig. 1.1 Idealized View of Nearshore RIB Concept (Melby and Resio 2002)

2 EXPERIMENTS

2.1 Experimental Setup

A small-scale physical model study was conducted by Melby and Resio (2002) to investigate the functional and structural response of the nearshore RIB system in the U.S. Army Corps of Engineers, Coastal and Hydraulics Laboratory. The maximum anchor loads and the resulting tensile loads in the fabric shroud were measured in their study. In addition, the functional performance of the structure, defined primarily by wave transmission, was measured. The structure and anchor loads and the functional performance were anticipated to be a strong function of the structure geometry defined by the crest height or freeboard, the seaward slope of the shroud, the cross-shore width of the structure, and the freespan length of the shroud, as well as the incident wave conditions and water level. Their experiments are summarized in the following.

In their conceptual study, various structure configurations were tested including a single tube structure and a two-tube structure, both with varied freeboard. The study was conducted in a wave flume that was 0.91 m wide, 0.91 m deep, and 45 m long. The 0.91-m-wide flume width was divided into two channels, one 0.61 m wide and the other 0.30 m wide. The structure was constructed to span the 0.61-m-wide flume while the 0.30-m-wide flume was left open in order to measure incident waves unaffected by the structure.

Irregular waves were generated using the TMA spectrum with the spreading parameter of 3.3 by a piston-type wave maker. Each 15-min time series was generated using a random phase method. In this technique, the phases of the Fourier components are chosen at random but the amplitudes are set deterministically according to the target spectrum. The resulting wave records have spectra that exactly match the target spectrum. The maximum and minimum frequencies were set to 3.0 and 0.1 Hz, respectively.

Waves shoaled up with a uniform slope of 1:82. Water surface elevations were measured at 9 locations in the flume. Fig. 2.1 shows the flume layout with the wave gage locations. Two gage arrays, consisting of 3 gages each, were placed in shallow water and deep water. In the gage arrays, the seaward two gages were separated by 0.305 m while the two landward gages were separated by 0.610 m. There were two gages placed 2.22 m and 3.00 m directly landward of the structure toe and one gage located in the open channel coincident with the structure toe. The wave data were collected at 50 Hz for 590 sec from the 15-min wave generation. A total of 30 seconds was removed from the start of each wave record. Tables 1 and 2 list model test parameters for the three plans tested. In Tables 1 and 2, the depth at the structure toe was measured at the point where the seaward slope would intersect the bottom. The freeboard is defined as the distance from the still water level to the crest of the largest cylinder as shown in Fig. 2.2.

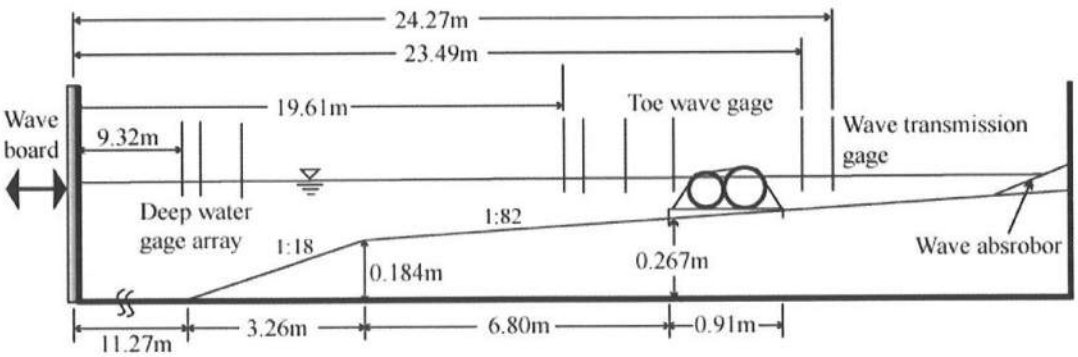

Fig. 2.1 Wave Flume Layout with Structure and Wave Gage Locations

The structure was anchored to an aluminum plate that was bolted to the concrete floor as shown in Fig. 2.2 where the 7.6 cm-deep sand layer placed on the concrete floor to avoid sudden depth changes is not shown in this and subsequent figures. The structure spanned the full width of the 0.61-m-wide flume. The tubes were constructed of PVC pipe and were effectively infinitely stiff compared to the shroud. The tubes were free to move under the shroud. The shroud was sandwiched in a spreader plate on both ends, each spreader plate consisting of two 1-mm-thick aluminum plates.

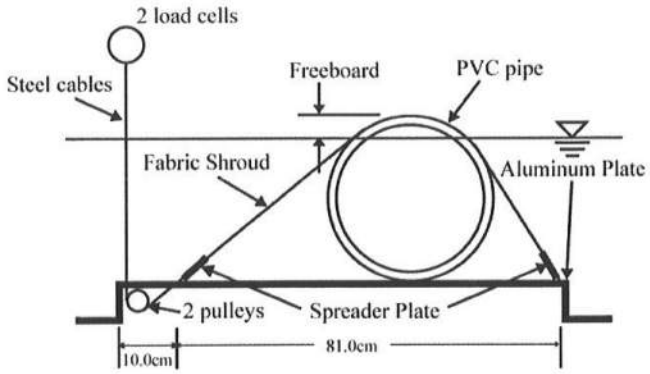

Fig. 2.2 Shore-RIB Layout and Support Configuration

The spreader plates were 3.9 cm wide and spanned the full width of the flume. The shoreward plate connection was connected to the base plate using 4 shackles. The seaward end was connected to two 1 mm diameter steel cables which ran through the steel plate, around pulleys, and back up to the 2 load cells that were mounted to a rigid support structure above the model. Using this setup, the sum of the measured forces in the two load cells would be equivalent to the total longitudinal force in the fabric. The model shroud material was a 284-gram polyester with approximate thickness of 0.25 mm.

Forces in the fabric shroud were measured using 2 load cells. The preload in the fabric shroud was used to cause the static tension in the fabric shroud. The tension force per unit width in N/m was the sum of the two load cell forces divided by the width of the flume (0.61 m). Values were given for both pre-test and post-test loads. The movement of the tube(s) during the test caused the preload to decrease, for the high preload cases, or increase for the low preload cases, although some tests deviated from this. The average of the pre-test and post-test loads is used here to obtain the static tension force per unit width for each test.

2.2 Measurements

A spectral analysis of each wave gage record was performed. The spectral density was obtained by smoothing the modified periodogram of each record. A cosine bell data window with nondimensional length of 0.1 was used to reduce leakage. The modified periodogram was smoothed using a moving average filter with filter length set to obtain a filter bandwidth of 0.05 Hz. The high and low frequency cutoffs were 3.0 and 0.1 Hz, respectively. The resulting spectral significant wave height was used to describe the wave height. It is defined as $H_{mo}' = 4m_0^{1/2}$ with m_0=zero moment of the wave spectrum. The spectral peak period is defined as $T_p' = 1/f_p'$ where f_p' is the frequency at the spectral peak. The prime is used to indicate the dimensional variables. The wave height and period in Table.1 and 2 are those measured in the open flume at the structure toe. The toe water depth, h', freeboard, R_c', incident wave height, H_{mo}', wave period, T_p', and fabric pre-tension were all varied systematically in order to define the response of the system over a wide range of wave and pre-tension conditions.

Three different structure plans were tested. Fig. 2.3 shows Plan 1. This plan consisted of a 32.3-cm diameter PVC tube that was free to roll and slide under the fabric shroud. A 94-N weight was placed inside the tube. The tube was open on the ends and therefore filled with water to the still water level. Fig. 2.4 shows Plan 2. This plan was similar to Plan 1 except the weight was removed from inside the tube and small wood chocks were added to either side of the tube to prevent rolling. Fig. 2.5 shows Plan 3. In this

plan, the single 32.3-cm tube was replaced by two tubes with diameters 21.8 cm and 27.5 cm. The largest tube was on the landward side of the structure. For plan 3, both tubes included wood chocks to prevent rolling.

For all plans, the tests consisted of a series of different waves and water levels. In addition, each test was run with low and high pre-tensions in the fabric shroud. The fabric shroud was preloaded by tightening turnbuckles that connected the anchor lines to the load cells. The low pre-tension was roughly 5 N in each load cell, which was the lowest possible to prevent flapping of the shroud. The high pre-tension was approximately 40 N in each load cell. Table 2.1 and 2.2 list the static tension force per unit width, T_s', for each test.

When testing Plan 1, the tube oscillated seaward and landward approximately 18 cm during the tests with low preload. This movement occurred partly because the tests were begun with the tube in its furthest landward position. The tube always migrated toward the geometric center of the structure with significant oscillations about the center primarily as a function of wave period and the phasing of the waves. The tube movement was reduced to 9 cm with high preload and with the tube placed initially in the center position. For Plans 2 and 3, the lateral excursion was much lower for both the low and high preload cases, primarily due to the addition of wooden chocks connected to the base of the PVC tubes. These chocks crudely simulated the resistance to sliding and rolling that would be present in the prototype structure because the prototype fabric tubes would assume an oblate shape on the bottom of the ocean. For Plan 2, all tests began with the tube in the center and the maximum excursion was about 5 cm for all tests. For Plan 3, all tests began with the contact point between the two tubes placed at the center of the structure and the maximum lateral excursion ranged from 0 to 2.5 cm.

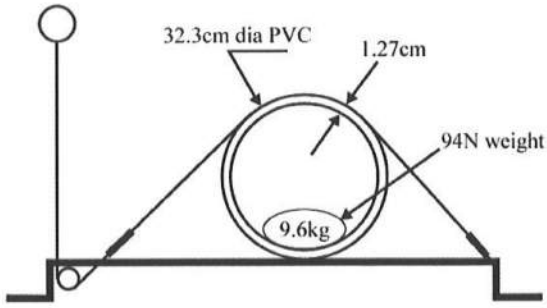

Fig. 2.3 Cross-sectional Layout of Plan 1 Structure

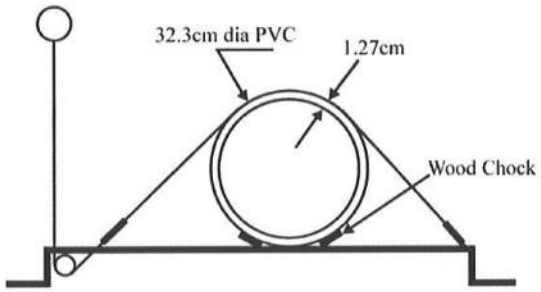

Fig. 2.4 Cross-sectional Layout of Plan 2 Structure

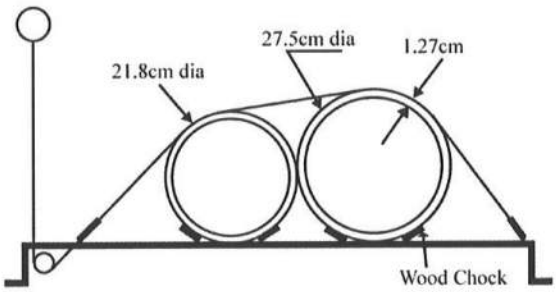

Fig. 2.5 Cross-sectional Layout of Plan 3 Structure

Table 2.1 and 2.2 list the wave transmission coefficient and measured maximum tension in the fabric. The wave transmission coefficient is defined as $K_t=(H_{mo}')_t/(H_{mo}')_i$, where $(H_{mo}')_t$ is the transmitted spectral significant wave height and $(H_{mo}')_i$ is the corresponding incident wave height. The maximum fabric tension force per unit width, T_{max}', is the sum of the maximum force in each load cell divided by the width of the flume. It is noted that the wave transmission coefficients measured at the two locations in Fig. 2.1 were found to be practically the same. Hence, the average value for each test is listed in Table 2.1 and 2.2

Table 2.1 Wave Conditions, Transmission Coefficient, Static and Maximum Tension for Plans 1 and 2

Test	Depth at Toe h'(cm)	Freeboard R_c'(cm)	Incident Wave Period T_p'(sec)	Incident Wave Height H_{mo}'(cm)	Tranmission Coefficient K_t	Static Tension T_s'(N/m)	Maximum Tension T_{max}'(N/m)
1.1	29.4	2.9	1.4	11.3	0.67	0.0	382.3
1.2			2.1	12.1	0.71	0.0	393.1
1.3			1.7	11.6	0.71	0.0	413.6
1.4			1.4	11.3	0.64	68.9	327.2
1.5			1.4	11.7	0.51	97.9	341.0
1.6			1.3	11.6	0.48	169.8	281.0
1.7			1.9	12.5	0.49	135.6	370.8
1.8			2.0	12.9	0.47	138.2	413.4
1.9			1.5	12.2	0.48	136.9	313.8
1.10			2.1	12.5	0.52	132.8	457.0
1.11			2.6	12.9	0.53	126.4	487.2
1.12			2.7	13.5	0.51	143.4	519.0
2.1			1.4	12.0	0.47	124.1	225.7
2.2			1.7	12.3	0.51	124.1	289.3
2.3			2.2	12.8	0.49	124.1	313.1
2.4			1.4	11.7	0.47	14.8	211.0
2.5			1.7	12.3	0.49	14.8	310.0
2.6			2.2	12.9	0.47	14.8	419.2

Table 2.2 Wave Conditions, Transmission Coefficient, Static and Maximum Tension for Plans 3

Test	Depth at Toe h'(cm)	Freeboard R_c'(cm)	Incident Wave Period T_p'(sec)	Incident Wave Height H_{mo}'(cm)	Tranmission Coefficient K_t	Static Tension T_s'(N/m)	Maximum Tension T_{max}'(N/m)
3.1	24.6	2.9	1.3	9.8	0.41	119.7	163.1
3.2			1.4	9.8	0.44	126.2	162.5
3.3			1.7	9.7	0.46	126.2	165.1
3.4			1.7	9.8	0.49	124.8	174.1
3.5			2.0	9.6	0.49	127.2	162.0
3.6			2.3	10.0	0.48	129.7	154.9
3.7			2.4	10.1	0.50	131.0	160.3
3.8			1.3	9.6	0.40	14.9	82.1
3.9			1.4	9.9	0.42	15.7	88.7
3.10			1.7	9.8	0.43	14.9	87.5
3.11			1.7	9.8	0.46	14.8	97.9
3.12			2.0	9.6	0.47	15.7	89.8
3.13			2.3	10.0	0.46	14.9	97.9
3.14			2.4	10.4	0.47	14.9	108.0
3.15	30.2	-2.7	1.3	11.3	0.59	104.4	171.5
3.16			1.7	12.4	0.60	133.6	177.9
3.17			2.2	12.0	0.63	132.1	169.7
3.18			2.3	12.7	0.63	139.3	174.3
3.19			2.3	12.9	0.65	140.8	177.9
3.20			1.2	11.3	0.53	22.6	140.7
3.21			1.7	12.5	0.55	33.6	148.5
3.22			2.2	12.0	0.60	34.3	168.0
3.23			2.3	12.4	0.61	55.4	183.4
3.24			2.4	12.6	0.62	17.4	149.5
3.25	19.8	7.7	1.2	7.7	0.23	119.0	133.8
3.26			1.6	8.1	0.27	119.0	128.4
3.27			2.1	7.9	0.29	115.2	143.1
3.28			2.2	8.1	0.31	124.1	157.9
3.29			2.6	8.1	0.32	126.2	148.0
3.30			1.4	9.1	0.27	126.2	161.8
3.31			1.6	9.7	0.31	133.6	164.9
3.32			2.1	9.6	0.32	131.5	165.9
3.33			2.2	9.6	0.33	131.5	160.5
3.34			2.6	9.6	0.33	131.5	149.0
3.35			1.4	10.1	0.28	119.0	152.0
3.36			1.6	10.5	0.33	119.0	168.7
3.37			2.1	10.2	0.35	130.0	162.0
3.38			2.2	10.1	0.35	133.0	158.9
3.39			2.6	10.2	0.35	135.1	161.8
3.40			1.4	9.8	0.26	29.2	84.6
3.41			1.6	10.2	0.30	34.9	101.0
3.42			2.1	10.0	0.30	41.7	107.9
3.43			2.2	10.1	0.31	41.6	119.5
3.44			2.6	10.1	0.32	39.3	113.3

3 NUMERICAL MODEL

The numerical model adopted in this study is explained in this chapter. The governing equations, numerical method and computational procedures are expressed in Chapter 3.1. The computation methods for wave reflection, wave transmission and energy balance are described in Chapter 3.2. The computation method for predicting the wave force is derived in Chapter 3.3.

3.1 Governing Equations and Numerical Method

3.1.1 Governing equations

In order to predict the irregular wave motion and resulting force on the Shore-RIB structure, the numerical model developed by Kobayashi and Wurjanto (1989) is modified here. The wave motion on the structure, which is assumed to be impermeable and stationary, is computed for the irregular incident wave specified at the seaward boundary of the computation domain as shown in Fig. 3.1. The landward boundary located at $x'=x_e'$ is also shown. The prime indicates the dimensional variables in the following. The symbols shown in Fig. 3.1 are as follows: x'=horizontal coordinate taken to be positive landward with $x'=0$ at the seaward boundary; z'=vertical coordinate taken to be positive upward with $z'=0$ at the still water level (SWL); d_t'=water depth below SWL at the seaward boundary; d_e'=water depth below SWL at the landward boundary; θ'=local angle of the slope which may vary along the slope; η'=free surface elevation above SWL; h'=water depth above the impermeable slope; and u'=depth-averaged horizontal velocity. Kobayashi and Wurjanto (1989) computed wave transmission over a submerged structure as shown in Fig. 3.1. Their numerical model is extended here to compute wave transmission over both emerged and submerged structures.

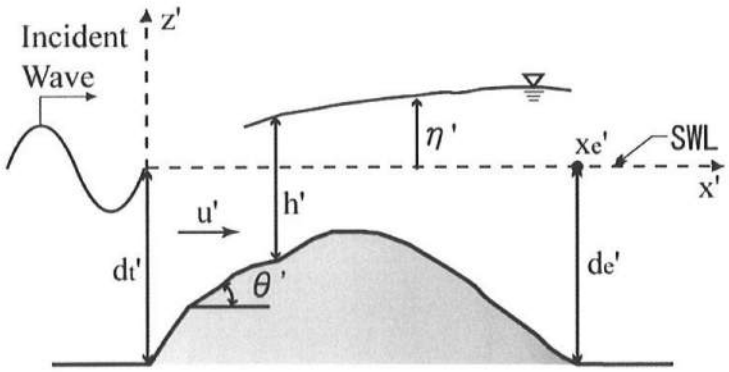

Fig. 3.1 Definition Sketch

For the flow over the impermeable structure, the vertically-integrated equations for mass and x'-momentum for finite-amplitude shallow-water waves are expressed as (Kobayashi et al.,1987)

$$\frac{\partial h'}{\partial t'}+\frac{\partial}{\partial x'}(h'u')=0 \tag{3.1}$$

$$\frac{\partial}{\partial t'}(h'u')+\frac{\partial}{\partial x'}(h'u'^2)=-gh'\frac{\partial \eta'}{\partial x'}-\frac{1}{2}f'|u'|u' \tag{3.2}$$

where t'=time; g=gravitational acceleration; and f'=constant friction factor related to the shear stress acting on the structure. Use is made of $f'=0$ in the following computations because the surface of the fabric shroud is smooth and essentially impermeable.

The following dimensionless variables and parameters are introduced to normalize Eqs. (3.1) and (3.2):

$$t = t'/T_r' \;;\; x = x'/[T_r'(gH_r')^{1/2}] \;;\; u = u'/(gH_r')^{1/2} \tag{3.3}$$

$$z = z'/H_r' \;;\; h = h'/H_r' \;;\; \eta = \eta'/H_r' \;;\; d_t = d_t'/H_r' \tag{3.4}$$

$$\sigma = T_r'(g/H_r')^{1/2} \;;\; \theta = \sigma \tan\theta' \;;\; f = \sigma f'/2 \tag{3.5}$$

where T_r'=representative wave period; H_r'=representative wave height; σ=parameter expressing the ratio between the horizontal and vertical length scales; θ=dimensionless gradient of the slope; and f =normalized friction factor. In the following computation, use is made of $T_r' = T_p'$ and $H_r' = H_{mo}'$ where T_p'= incident wave spectral peak period and H_{mo}'= incident wave spectral significant wave height. The representative wave period and height used for the normalization can be taken as the period and height used to characterize the incident wave for a particular problem.

Substitution of Eqs. (3.3)-(3.5) into Eqs. (3.1) and (3.2) yields

$$\frac{\partial h}{\partial t} + \frac{\partial}{\partial x}(hu) = 0 \tag{3.6}$$

$$\frac{\partial}{\partial t}(hu) + \frac{\partial}{\partial x}(hu^2 + \frac{1}{2}h^2) = -\theta h - f|u|u \tag{3.7}$$

where θ and f express the effect of the slope and friction, respectively. In term of the normalized coordinate system, the slope is located at

$$z = \int_0^x \theta dx - d_t \;;\; x \geq 0 \tag{3.8}$$

which reduces to $z = (\theta x - d_t)$ for a uniform slope.

3.1.2 Numerical method

The initial time t=0 for the computation marching forward in time is taken to be the time when the specified incident wave train arrives at the seaward boundary located at x=0 as shown in Fig. 3.1. The initial conditions for the computation are thus given by η=0 and u=0 in the region $x \geq 0$. It is noted that h and η are uniquely related for given slope geometry expressed by Eq.(3.8).

Eqs.(3.6) and (3.7) are combined and expressed in the following vector form:

$$\frac{\partial \boldsymbol{U}}{\partial t} + \frac{\partial \boldsymbol{F}}{\partial x} + \boldsymbol{G} = 0 \tag{3.9}$$

with $$\boldsymbol{U} = \begin{bmatrix} m \\ h \end{bmatrix} \;;\; \boldsymbol{F} = \begin{bmatrix} mu + 0.5h^2 \\ m \end{bmatrix} \;;\; \boldsymbol{G} = \begin{bmatrix} \theta h + f|u|u \\ 0 \end{bmatrix} \tag{3.10}$$

where m=uh is the normalized volume flux per unit width. The vectors $\boldsymbol{F}$ and $\boldsymbol{G}$ depend on the vector $\boldsymbol{U}$ for given θ and f.

Eq. (3.9) is discretized using a finite difference grid of constant space size Δx and constant time step Δt based on an explicit dissipative Lax-Wendroff method. In the following, the known quantities at the node located at $x=(j\text{-}1)\,\Delta x$ ($j=1,2,\ldots,je$) and at the time $t=(n\text{-}1)\Delta t$ are indicated by the subscript j without a superscript. The integer je indicates the landward boundary node located at $x = x_e$. The unknown quantities at the node j and at the time $t=n\Delta t$ are denoted by the subscript j with the superscript * where the asterisk indicates the quantities at the next time level. The values of $\boldsymbol{U}_1$* and $\boldsymbol{U}_{je}$* are computed using the seaward and landward boundary conditions, respectively. The values of $\boldsymbol{U}_j$* for $j=2,3,\ldots$, (je-1) are computed using the known values of $\boldsymbol{U}_{j-1}$, $\boldsymbol{U}_j$ and $\boldsymbol{U}_{j+1}$ at the time $t=(n\text{-}1)\Delta t$ (Kobayashi et al., 1987)

$$\boldsymbol{U}_j^* = \boldsymbol{U}_j - \lambda\left[\frac{1}{2}(\boldsymbol{F}_{j+1} - \boldsymbol{F}_{j-1}) + \Delta x \boldsymbol{G}_j\right] + \frac{\lambda^2}{2}(\boldsymbol{g}_j - \boldsymbol{g}_{j-1} - \Delta x \boldsymbol{S}_j) + \boldsymbol{D}_j \tag{3.11}$$

where $\lambda=\Delta t/\Delta x$ and if the computed value of h_j* turns out to be negative, use is made of $h^* = 0$, $u_j^* = 0$ and $m_j^* = 0$ to account for possible dry nodes on the structure. The vector $\boldsymbol{g}_j$ in Eq. (3.11) is given by

$$\boldsymbol{g}_j = \frac{1}{2}(\boldsymbol{A}_{j+1} + \boldsymbol{A}_j)\left[\boldsymbol{F}_{j+1} - \boldsymbol{F}_j + \frac{\Delta x}{2}(\boldsymbol{G}_{j+1} + \boldsymbol{G}_j)\right] \tag{3.12}$$

with $$\boldsymbol{A} = \begin{bmatrix} 2u & ; & (h-u^2) \\ 1 & ; & 0 \end{bmatrix} \tag{3.13}$$

The vector $\boldsymbol{S}_j$ in Eq. (3.11) is defined as

$$\boldsymbol{S}_j = \begin{bmatrix} \Delta x e_j - 0.5\theta_j\,(m_{j+1} - m_{j-1}) \\ 0 \end{bmatrix} \tag{3.14}$$

with $$e_j = \frac{2f|u_j|}{h_j}\left[\frac{(u_j^2 - h_j)(h_{j+1} - h_{j-1})}{(2\Delta x)} - \frac{u_j(m_{j+1} - m_{j-1})}{(2\Delta x)} - \theta_j h_j - f|u_j|u_j\right] \tag{3.15}$$

where h_j in the denominator on the right hand side of Eq.(3.15) is replaced by $\delta = 0.001$ if $0 \le h_j < \delta$ to avoid the division by a very small number.

The vector $\boldsymbol{D}_j$ in Eq. (3.11) represents the additional term for damping high frequency parasitic waves, which tend to appear at the rear of a breaking wave, and is given by

$$\boldsymbol{D}_j = \frac{\lambda}{2}\left[\boldsymbol{Q}_j(\boldsymbol{U}_{j+1} - \boldsymbol{U}_j) - \boldsymbol{Q}_{j-1}(\boldsymbol{U}_j - \boldsymbol{U}_{j-1})\right] \tag{3.16}$$

with $$\boldsymbol{Q}_j = p_j \boldsymbol{I} + \frac{1}{2} q_j (\boldsymbol{A}_j + \boldsymbol{A}_{j+1}) \tag{3.17}$$

where $\boldsymbol{I}$ = unit matrix; and the coefficients p_j and q_j are given by

$$p_j = \frac{1}{2}\frac{\left[\varepsilon_2\left|w_{j+1}-w_j\right|\left(v_j+v_{j+1}\right)-\varepsilon_1\left|v_{j+1}-v_j\right|\left(w_j+w_{j+1}\right)\right]}{\left(c_j+c_{j+1}\right)} \tag{3.18}$$

$$q_j = \frac{\left[\varepsilon_1\left|v_{j+1}-v_j\right|-\varepsilon_2\left|w_{j+1}-w_j\right|\right]}{\left(c_j+c_{j+1}\right)} \tag{3.19}$$

with $\quad c = h^{1/2} \quad ; \quad v = u + c \quad ; \quad w = u - c$ (3.20)

where ε_1 and ε_2 are positive damping coefficients determining the amount of numerical damping of high frequency parasitic waves at the rear of a breaking wave. The denominator (c_j+c_{j+1}) on the right hand sides of Eqs. (3.18) and (3.19) is replaced by $\delta = 0.001$ if $0 \le (c_j + c_{j+1}) < \delta$.

The numerical stability criterion for this explicit finite difference method is given by

$$\frac{\Delta t}{\Delta x} < \frac{\left[\left(1+\frac{\varepsilon^2}{4}\right)^{1/2}-\frac{\varepsilon}{2}\right]}{\left(\left|u_m\right|+c_m\right)} \tag{3.21}$$

where u_m=maximum value of u expected to be encountered in the flow field; c_m=maximum expected value of $h^{1/2}$; and ε=greatest coefficient of ε_1 and ε_2.

3.1.3 Computational parameters and procedure

The values of Δt, Δx, ε_1 and ε_2 used in the following computation are discussed below. The dimensional grid spacing $\Delta x'$=0.5 *cm* is used to resolve the spatial variation of the breaking wave whose height is on the order of 10 cm. The number of grids along the x-axis is 163 for each case as will be explained in Chapter 4. The normalized time step Δt is 1/3300-1/3000 to resolve the rapid temporal variation of the breaking wave and to satisfy Eq.(3.21). The damping coefficients ε_1 and ε_2 are taken as $\varepsilon_1 = \varepsilon_2 = 2.0$ as recommended by Kobayashi and Wurjanto (1989) for computing regular wave transmission over a submerged trapezoidal breakwater.

As summarized in Fig. 3.2, the computation procedure is explained as follows:

1. Input the structure geometry, computation parameters, and initial conditions as well as the measured incident irregular wave profile at the seaward boundary at the beginning of each

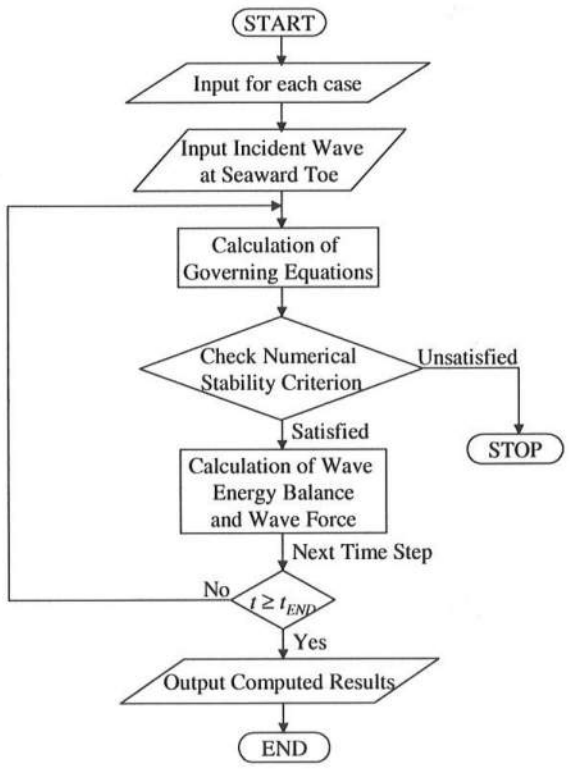

Fig. 3.2 Computation Procedure

computation.

2. Perform the time marching computation using Eq. (3.11) and the boundary algorithms which will be explained in Chapter 3.2.
3. Check whether the numerical stability criterion given by Eq. (3.21) is satisfied or not. The computation stops if it is not satisfied.
4. Calculate the wave energy balance which will be explained in Chapter 3.2, and the wave force acting on the Shore-RIB structure as will be explained in Chapter 3.3.
5. Continue the computation for the specified duration.
6. Store the computed results for output.

3.1.4 Incident wave profile

The measured temporal variation of $\eta_i'(t)$ from each of the laboratory tests conducted by Melby and Resio (2002) is normalized and specified as input for the incident wave. The measured time series for the duration of 30-590 s sampled at the rate of 0.02 s is used for the computation by removing the initial transition of 30 s. The computation duration is hence for $t' = 0 - 560$ s. A linear interpolation of the input time series is employed to obtain the value of $\eta_i(t)$ at each time step because the time step Δt is much less than the data sampling rate of 0.02 s.

The initial conditions for the computation requires no wave at the initial time t=0. A smooth transition over the first wave period is introduced using a sine function with $\eta_i = 0$ at t=0 to satisfy the initial condition.

3.2 Wave Reflection, Transmission and Energy Balance

In order to derive appropriate seaward and landward boundary conditions, Eqs. (3.6) and (3.7) are expressed in the following characteristic forms

$$\frac{\partial \alpha}{\partial t} + (u+c)\frac{\partial \alpha}{\partial x} = -\theta - \frac{f|u|u}{h} \quad ; \quad \frac{dx}{dt} = u + c \tag{3.22}$$

$$\frac{\partial \beta}{\partial t} + (u-c)\frac{\partial \beta}{\partial x} = \theta + \frac{f|u|u}{h} \quad ; \quad \frac{dx}{dt} = u - c \tag{3.23}$$

with $\quad c = h^{1/2} \quad ; \quad \alpha = u + 2c \quad ; \quad \beta = -u + 2c$ (3.24)

where α and β are the characteristic variables.

3.2.1 Wave reflection

Assuming that $u < c$ in the vicinity of the seaward boundary where the normalized water depth below SWL is d_t, α and β represent the characteristics advancing landward and seaward, respectively, in the vicinity of the seaward boundary. The total water depth at the seaward boundary is expressed in the form (Kobayashi et al. 1987)

$$h = d_t + \eta_i(t) + \eta_r(t) \qquad \text{at} \quad x = 0 \tag{3.25}$$

where η_i and η_r are the free surface variations normalized by H_r' at x=0 due to the incident and reflected waves, respectively. The incident wave train is specified by prescribing the variation of η_i with respect to $t \geq 0$. The normalized reflected wave train η_r is approximately expressed in terms of the seaward advancing characteristic β at x=0

$$\eta_r(t) \cong \frac{1}{2} d_t^{1/2} \beta(t) - d_t \quad \text{at} \quad x = 0 \tag{3.26}$$

where β is given by Eq. (3.23).

It is also required to find the unknown value of the vector $\boldsymbol{U}_1$* at x=0 and the time $t=n\Delta t$ which cannot be computed using Eq. (3.11).

A simple first-order finite difference equation corresponding to Eq. (3.23) with f=0, where the bottom friction is negligible in finite depth, is used to find the value of β_1* at x=0 and the time $t=n\Delta t$

$$\beta_1^* = \beta_1 - \frac{\Delta t}{\Delta x}(u_1 - c_1)(\beta_2 - \beta_1) + \Delta t \theta_1 \tag{3.27}$$

where $\beta_1 = (-u_1 + 2c_1)$ and $\beta_2 = (-u_2 + 2c_2)$.

The right hand side of Eq. (3.27) can be computed for the known values of $\boldsymbol{U}_j$ with j=1 and 2 at the time $t=(n\text{-}1)\Delta t$ where the spatial nodes are located at $x = (j-1)\Delta x$. The value of η_r at the time $t=n\Delta t$ is calculated using Eq. (3.26). Eq. (3.25) yields the value of h_1*, while $u_1^* = [2(h_1^*)^{1/2} - \beta_1^*]$ using the definition of β given in Eq. (3.24). Thus, the values of h_1*, u_1* and m_1*=u_1*h_1* at x=0 and $t = n\Delta t$ are obtained.

The reflection coefficient K_r at x=0 is estimated as the ratio of the reflected wave standard deviation and the incident wave standard deviation

$$K_r = \left[\frac{\overline{(\eta_r - \overline{\eta_r})^2}}{\overline{\eta_i^2}} \right]^{1/2} \tag{3.28}$$

where the overbar indicates the time averaging for the entire computation duration. Eq.(3.28) accounts for the difference $\overline{\eta_r}$ between the still water level and the mean water level at x=0 where $\eta_i(t)$ is specified such that $\overline{\eta_i} = 0$.

3.2.2 Wave transmission

It is assumed that the transmitted waves at $x = x_e$ propagate landward without being reflected from the shoreline and the transmitted water flows landward without a return current. Assuming that $u<c$ in the vicinity of the landward boundary located at $x = x_e$ where the normalized water depth below SWL is $d_e=d_e'/H_r'$, α represents the characteristics advancing landward in the vicinity of the landward boundary. The boundary conditions at $x = x_e$ are expressed as (Kobayashi and Wurjanto 1989)

$$h = d_e + \eta_t(t) \quad \text{at} \quad x = x_e \tag{3.29}$$

$$\eta_t(t) = \frac{1}{2} d_e^{1/2} \alpha(t) - d_e \quad \text{at} \quad x = x_e \tag{3.30}$$

where η_t is the free surface oscillation at $x = x_e$ normalized by H_r' due to the transmitted wave. Eq. (3.30) expresses the transmitted wave train η_t in terms of the landward-advancing characteristic α given by Eq.(3.22) in a manner similar to Eq.(3.26) for the reflected wave train. U_{je}^* is computed in the following manner. A simple first-order finite difference equation corresponding to Eq. (3.22) with f=0, where the bottom friction is negligible in finite depth, is used to find the value of α_{je}* at $x = x_e$ and the time t=$n\Delta t$

$$\alpha_{je}^* = \alpha_{je} - \frac{\Delta t}{\Delta x}(u_{je} + c_{je})(\alpha_{je} - \alpha_{je-1}) - \Delta t \theta_{je} \tag{3.31}$$

where $\alpha_{je} = (u_{je} + 2c_{je})$ and $\alpha_{je-1} = (u_{je-1} + 2c_{je-1})$. α_{je}* is computed at t=$n\Delta t$ using Eq. (3.31) and η_t* at t=$n\Delta t$ using Eq. (3.30) with $\alpha = \alpha_{je}^*$. Then, h_{je}^* is computed as $h_{je}^* = (d_e + \eta_t^*)$ from Eq. (3.29), while $u_{je}^* = [\alpha_{je}^* - 2(h_{je}^*)^{1/2}]$. Thus, $m_{je}^* = h_{je}^* u_{je}^*$ and U_{je}^* is obtained.

The transmission coefficient K_t associated with the computed wave train $\eta_t(t)$ is estimated as the ratio of the transmitted wave standard deviation and the incident wave standard deviation assuming $d_{je} = d_t$.

$$K_t = \left[\frac{\overline{(\eta_t - \overline{\eta_t})^2}}{\overline{\eta_i^2}} \right]^{1/2} \tag{3.32}$$

The transmission coefficient $(K_t)_{mo}$ based on the ratio between the spectral transmitted significant wave height $(H_{mo})_t$ and the spectral incident significant wave height $(H_{mo})_i$ is defined as

$$(K_t)_{mo} = \frac{(H_{mo})_t}{(H_{mo})_i} \tag{3.33}$$

where $K_t = (K_t)_{mo}$ because H_{mo}=$4\sigma_\eta$ with σ_η = standard deviation of the time series of η used to compute the corresponding spectrum. On the other hand, the transmission coefficient $(K_t)_{1/3}$ is also computed as the ratio between the transmitted significant wave height $(H_{1/3})_t$ and the incident significant wave height $(H_{1/3})_i$

$$(K_t)_{1/3} = \frac{(H_{1/3})_t}{(H_{1/3})_i} \tag{3.34}$$

where the significant wave height $H_{1/3}$ is the average height of the highest 1/3 waves based on the zero-upcrossing method for the irregular wave profile. If the wave height distribution follows the Rayleigh distribution and linear wave theory is valid, the transmission coefficients defined above are expected to be the same.

3.2.3 Wave energy balance

The normalized equations of mass and x-momentum given by Eqs. (3.6) and (3.7) are used to compute

the flow field. The normalized energy equation corresponding to Eqs. (3.6) and (3.7) are expressed as (Kobayashi and Wurjanto 1989)

$$\frac{\partial E}{\partial t}+\frac{\partial}{\partial x}(E_F)=-D_f-D_B \tag{3.35}$$

with

$$E=\frac{1}{2}(hu^2+\eta^2) \qquad \text{for } h\geq\eta \tag{3.36a}$$

$$E=\frac{1}{2}[hu^2+\eta^2-(h-\eta)^2] \quad \text{for } h<\eta \tag{3.36b}$$

$$E_F=uh\left(\frac{u^2}{2}+\eta\right) \tag{3.37}$$

$$D_f=f|u|u^2 \tag{3.38}$$

where E =normalized specific energy defined as the sum of kinetic and potential energy per unit horizontal area; E_F =normalized energy flux per unit width; D_f =normalized rate of energy dissipation per unit horizontal area due to bottom friction; and D_B =normalized rate of energy dissipation per unit horizontal area due to wave breaking. The dimensional rate D_B' of energy dissipation due to wave breaking is given by $D_B'=(\rho g H_r'^2/T_r')D_B$ where ρ=fluid density, which is assumed to be constant neglecting air bubbles. The normalized potential energy is taken to be relative to the normalized potential energy at t=0 when the incident wave train arrives at x=0 as shown in Fig. 3.1. Eqs. (3.36a) and (3.36b) are applicable for the portion of the structure below and above SWL, respectively.

Since the wave energy balance is normally analyzed in terms of the time-averaged quantities, the time-averaged dissipation rate, $\overline{D_B}$ due to wave breaking is computed using the time-averaged energy equation derived from Eq. (3.35)

$$\overline{D_B}=-\frac{d}{dx}(\overline{E_F})-\overline{D_f} \tag{3.39}$$

The present numerical model needs to predict that $\overline{D_B}$ is positive or zero depending on whether wave breaking occurs or not. The energy flux $\overline{E_F}$ should decrease with the increase of x, while $\overline{D_f}\geq 0$ since D_f defined in Eq. (3.38) is positive or zero.

Integration of Eq. (3.39) from the seaward boundary to the landward boundary yields the time-averaged energy equation for the region $0\leq x\leq x_e$

$$\overline{E_F}(x=0)-\overline{E_F}(x=x_e)=\int_0^{x_e}(\overline{D_f}+\overline{D_B})dx \tag{3.40}$$

where the first and second terms on the left hand side of Eq. (3.40) are the values of $\overline{E_F}$ at $x=0$ and $x=x_e$, respectively. Eq. (3.40) implies that the difference between the net energy fluxes at the seaward

and landward boundaries equals the rate of energy dissipation between the two boundaries.

The specific energy $\overline{E}$ and the energy flux $\overline{E_F}$ at the seaward boundary, where $\eta=(\eta_i+\eta_r)$ at x=0 from Eq. (3.25), are approximately given by Kobayashi and Wurjanto (1989) using linear wave theory

$$\overline{E} \cong \overline{\eta_i^2} + \overline{(\eta_r - \overline{\eta_r})^2} \qquad \text{at } x=0 \tag{3.41}$$

$$\overline{E_F} \cong d_t^{1/2}\left[\overline{\eta_i^2} - \overline{(\eta_r - \overline{\eta_r})^2}\right] \qquad \text{at } x=0 \tag{3.42}$$

where $d_t^{1/2}$ is the normalized group velocity at x=0 based on linear long wave theory. The reflection coefficient K_r given by Eq. (3.28) including the effect of $\overline{\eta_r}$ is based on Eqs. (3.41) and (3.42).

On the other hand, the specific energy $\overline{E}$ and the energy flux $\overline{E_F}$ at the landward boundary, where $\eta=\eta_t$ at $x=x_e$, are approximated by use of linear wave theory

$$\overline{E} \cong \overline{(\eta_t - \overline{\eta_t})^2} \qquad \text{at } x=x_e \tag{3.43}$$

$$\overline{E_F} \cong d_e^{1/2}\overline{(\eta_t - \overline{\eta_t})^2} \qquad \text{at } x=x_e \tag{3.44}$$

where $d_e^{1/2}$ is the normalized group velocity at $x=x_e$ based on linear long wave theory. The transmission coefficient K_t given by Eq. (3.32) for the case of $d_e=d_t$ is based on Eqs. (3.43) and (3.44).

3.3 Wave Force

The horizontal and vertical wave forces on the entire Shore-RIB structure per unit width are predicted and used to estimate the measured fabric shroud tension per unit width.

The hydrostatic pressures on the upper and lower sides of the fabric shroud are balanced when there is no incident wave. The wave-induced pressure is assumed to act on the upper surface of the fabric shroud. The wave-induced pressure P_w' is hydrostatic below the instantaneous free surface elevation η' for finite-amplitude shallow-water waves

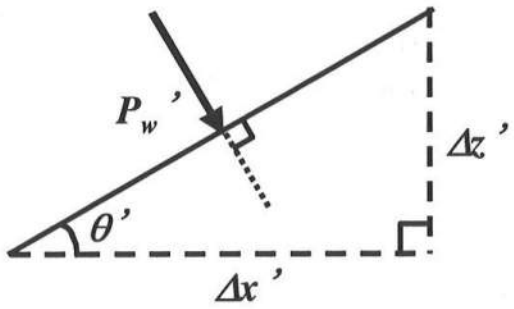

Fig. 3.3 Wave Pressure on Infinitesimal Structure Surface

$$P_w' \cong \rho g \eta' \tag{3.45}$$

where ρ =water density, g=gravitational acceleration, η'= dimensional free surface elevation above the Shore-RIB structure.

By the consideration of an infinitesimal surface of the fabric shroud with the length increments $\Delta x'$ and $\Delta z'=\tan\theta'\Delta x'$, and the surface length $[(\Delta x')^2+(\Delta z')^2]^{1/2}$ as shown in Fig. 3.3, the dimensional horizontal force $\Delta F_h'$ and the dimensional vertical force $\Delta F_v'$ are given by

$$\Delta F_h' = P_w' \sin\theta' \left[(\Delta x')^2 + (\Delta z')^2\right]^{1/2} \quad \text{(horizontal force)} \tag{3.46}$$

$$\Delta F_v' = P_w' \cos\theta' \left[(\Delta x')^2 + (\Delta z')^2 \right]^{1/2} \quad \text{(vertical force)} \tag{3.47}$$

with

$$\sin\theta' = \frac{\Delta z'}{\left[(\Delta x')^2 + (\Delta z')^2 \right]^{1/2}} = \frac{\tan\theta' \Delta x'}{\left[(\Delta x')^2 + (\Delta z')^2 \right]^{1/2}} \quad ; \quad \cos\theta' = \frac{\Delta x'}{\left[(\Delta x')^2 + (\Delta z')^2 \right]^{1/2}} \tag{3.48}$$

where the horizontal force is taken to be positive in the positive x'(landward) direction and the vertical force is taken to be positive downward.

Substitution of Eq. (3.48) into Eqs. (3.46) and (3.47) yields

$$\Delta F_h' = P_w' \tan\theta' \Delta x' \tag{3.49}$$

$$\Delta F_v' = P_w' \Delta x' \tag{3.50}$$

where the local bottom slope $\tan\theta'$ is known for the specified bottom geometry. The total dimensional horizontal force F_h' per unit width and the total dimensional vertical force F_v' per unit width in the region $0 \le x' \le x_e'$ are hence expressed as

$$F_h' = \int_0^{x_e'} P_w' \tan\theta' dx' \tag{3.51}$$

$$F_v' = \int_0^{x_e'} P_w' dx' \tag{3.52}$$

Substitution of Eq. (3.45) into Eqs. (3.51) and (3.52) yields

$$F_h' = \rho g \int_0^{x_e'} \eta' \tan\theta' dx' \tag{3.53}$$

$$F_v' = \rho g \int_0^{x_e'} \eta' dx' \tag{3.54}$$

The right hand side of Eqs. (3.53) and (3.54) are normalized by the dimensionless valuables defined in Eqs. (3.3)-(3.5)

$$F_h' = \rho g H_r'^2 \int_0^{x_e} \theta \eta dx \tag{3.55}$$

$$F_v' = \rho g H_r'^2 \sigma \int_0^{x_e} \eta dx \tag{3.56}$$

As a result, the, normalized horizontal force F_h per unit width and the normalized vertical force F_v per unit width are defined as

$$F_h = \frac{F_h'}{\rho g H_r'^2} = \int_0^{x_e} \theta \eta dx \tag{3.57}$$

$$F_v = \frac{F_v'}{\rho g H_r'^2 \sigma} = \int_0^{x_e} \eta dx \tag{3.58}$$

A simple trapezoidal rule is used for the numerical integration of Eqs. (3.57) and (3.58). $F_h(t)$ and $F_v(t)$ are computed as a function of time t using the computed free surface elevation $\eta(t,x)$ in the region $0 \le x \le x_e$ where the normalized bottom slope $\theta(x)$ in Eq. (3.57) is independent of t for the assumed stationary structure. The computed $F_h(t)$ and $F_v(t)$ will be used to estimate the fabric shroud tension per unit width using a simple quasi-static force balance equation for the Shore-RIB structure as illustrated in Fig. 3.4 that will be explained in Chapter 5.

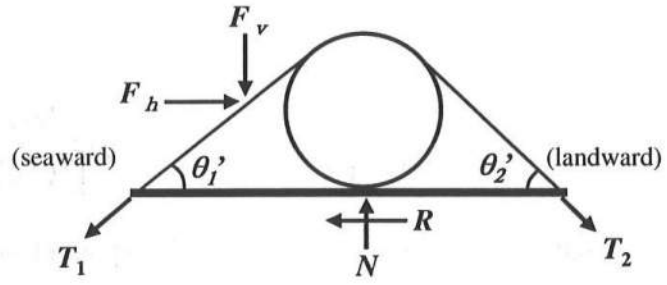

Fig. 3.4 Quasi-Static Force Balance

4 COMPUTED RESULTS

This chapter presents the computed results for six selected tests which include the free surface elevations at the seaward and landward boundaries, the free surface elevation and depth-averaged velocity and the energy balance. Six typical tests are selected for the computation as summarized in Chapter 4.1. The time series of the incident, reflected and transmitted waves are discussed in Chapter 4.2. The computed results of the free surface elevation and depth-averaged velocity are explained in Chapter 4.3 where the spectra of the measured transmitted waves are presented. Finally, the computed wave energy quantities are discussed in Chapter 4.4. The figures quoted in Chapters 4.2. 4.3 and 4.4 are attached in Appendix for convenience.

4.1 Six Tests Selected for Computation

The numerical model in Chapter 3 is compared with the 6 tests listed in Table 4.1 where the entire tests have been tabulated in Tables 2.1 and 2.2. The dimensionless parameters $d_t = d_t'/H_r'$, $x_e = x_e'/T_r'(gH_r')^{1/2}$ and $\sigma = T_r'(g/H_r')^{1/2}$, have been introduced in Eqs. (3.3)-(3.5), in which the prime indicates the dimensional variables, and d_t'=water depth below SWL at the seaward boundary as shown in Fig. 3.1; x_e'= horizontal distance of the computation domain; and H_r' = representative wave height taken as the spectral significant wave height; T_r' = representative wave period taken as the spectral peak period T_p'. The dimensionless parameters R_c, L and t_m in Table 4.1 are defined as $R_c = R_c'/H_r'$, $L = L'/d_t'$, and $t_m = t_m'/T_p'$ in which R_c=normalized freeboard defined as the distance above the still water level to the crest of the largest cylinder with $R_c<0$ for a submerged tube; L=normalized wave length at $x=0$; L'=wavelength at $x=0$ based on linear wave theory; t_m'=total computation duration taken as t_m'=560 s as explained in Chapter 3.1. Tests 1.3 and 2.2 correspond to one tube covered by the shroud, whereas Tests 3.5, 3.17, 3.22 and 3.32 involve two tubes as shown in Fig. 2.5. Although the physical model of Shore-RIB consists of the fabric shroud and mobile tubes, the Shore-RIB for the present numerical model is assumed to be rigid and impermeable.

Table 4.1 Summary of Six Tests Selected for Computation

Test	T_p' (s)	H_{mo}' (cm)	d_t	R_c	x_e	σ	L (=L'/d_t')	t_m
1.3	1.7	11.6	2.53	0.25	0.447	15.6	9.2	329.4
2.2	1.7	12.3	2.39	0.24	0.434	15.2	9.2	329.4
3.5	2.0	9.6	2.56	0.30	0.417	20.2	12.1	280.0
3.17	2.2	12.0	2.52	-0.23	0.339	19.9	12.0	254.5
3.22	2.2	12.0	2.52	-0.23	0.339	19.9	12.0	254.5
3.32	2.1	9.6	2.06	0.80	0.397	21.2	14.3	266.7

4.2 Waves at Seaward and Landward Boundaries

Figs. A.1(a)-(f) in Appendix show the normalized time series of the measured incident wave train $\eta_i(t)$, the computed reflected wave train $\eta_r(t)$, the total wave train $\eta_{tot}(t)=[\eta_i(t)+\eta_r(t)]$ at the seaward boundary $x=0$ and the computed transmitted wave train $\eta_t(t)$ at the landward boundary $x=x_e$ for each test. The horizontal axis t in each figure is the normalized time defined as the dimensional time t' divided by the

peak period T_p'. The seaward boundary condition using the measured incident wave profile $\eta_i(t)$ has been explained in Chapter 3.1. The computation duration for each test is $0 \le t \le t_m$ and the time series in Figs. A.1 are at the end of the computation.

For Tests 1.3, 2.2, 3.5 and 3.32 for the emerged breakwaters, the transmitted waves are related to wave overtopping. Therefore, the transmitted wave trains for these tests show sharp peaks of overtopping waves. The transmitted waves may become undular as they propagate. The development of an undular bore was predicted numerically by Peregrine(1966) using a Boussinesq wave model for the case of no wave breaking. The present numerical model based on finite-amplitude, shallow-water waves cannot predict the development of an undular bore because wave dispersion is not accounted for.

Figs. A.2(a)-(f) in Appendix show the computed spectra of η_i at x=0 and η_t at $x=x_e$. These normalized spectra are plotted as a function of the normalized frequency, $f = f' T_p'$, where f'= dimensional frequency. The spectra shown in each figure are the smoothed spectra with 16 degrees of freedom. The incident wave spectrum corresponds to the measured incident wave profile at the seaward toe of the structure where the incident waves were generated using the TMA spectrum as explained in Chapter 2.1. The computed transmitted wave spectrum is compared with the measured transmitted wave spectrum for each test where the location of the transmitted wave measurement depicted in Fig. 2.1 is farther landward of $x=x_e$.

For Test 1.3, the difference between the measured η_i and the measured η_t is relatively small because of large transmitted waves due to no shroud pre-tension and tube oscillations. For Test 2.2, there is a relatively larger difference between the measured η_i and η_t because the tube was essentially fixed by the wooden chocks as explained in relation to Figs. 2.3 and 2.4. The spectrum of the computed η_t is smaller than the measured spectrum for η_t around the peak frequency for both tests.

For Tests 3.17 and 3.22, the agreement between the computed and measured spectra for η_t is reasonable probably because these tests correspond to the submerged Shore-RIB structures and more waves were transmitted than in the other tests for the emerged Shore-RIB structures.

For Test 3.5, the difference between the computed and measured spectra for η_t is noticeable at the peak frequency, f=1, and at the low frequency, f~0.2.

For Test 3.32, the disagreement between the computed and measured spectra for η_t at the peak frequency and low frequency is large like Test 3.5. The larger difference between the spectra for η_i and η_t implies the smaller wave transmission and larger wave energy dissipation due to the greater R_c of this highly emerged breakwater.

In Figs. A.2, the power spectra of the measured η_t in the low frequency range f~0.2 are relatively large for every test. The reason may be related to wave groups of large waves overtopping the structure. The tubes constrained by the wood chocks oscillated intermittently in the cross-shore direction, and this slight movement might also have generated low-frequency waves.

4.3 Free Surface Elevation and Depth-averaged Velocity

Figs. A.3(a)-(f) in Appendix show the spatial variations of the computed maximum, mean and minimum free surface elevation η above the normalized Shore-RIB structure, where the actual tube was circular, as well as the spatial variations of the computed maximum, mean and minimum depth-averaged horizontal velocity u. The maximum, mean and minimum values of η and u are obtained from the computed time series during the entire duration $0 \le t \le t_m$.

For all the tests the mean free surface elevation at the seaward boundary, x=0, is slightly negative and that at the landward boundary, $x=x_e$, is slightly positive. This is caused by wave set-down and wave setup

due to the occurrence of wave breaking above the Shore-RIB structure in the computation domain. The numerical model predicts the mean surface elevation $\overline{\eta_r}$ at x=0 on the order of −0.03 and the value of $\overline{\eta}$ at $x=x_e$ on the order of 0.03 for all the tests. It should be noted that the incident wave profile $\eta_i(t)$ specified as input has zero mean. As a result, the wave set-down is the same as the computed mean value $\overline{\eta_r}$ of the reflected wave and the wave set-up is the computed mean value $\overline{\eta_t}$ of the transmitted wave.

The normalized mean water level difference, that is, the difference between the wave setup $\overline{\eta_t}$ at $x= x_e$ and the wave set-down $\overline{\eta_r}$ at x=0 is expressed as

$$\Delta\overline{\eta} = \overline{\eta_t} - (\overline{\eta_i} + \overline{\eta_r}) = \overline{\eta_t} - \overline{\eta_r} \tag{4.1}$$

The computed difference $\Delta\overline{\eta}$ is in the range of 0.03-0.10 for the six tests. Fig. 4.1 shows the computed values of $\Delta\overline{\eta}$ as a function of the normalized freeboard R_c. The comparison of the computed and empirical values of the mean water level difference for submerged breakwaters was presented by Kobayashi and Wurjanto (1989), but no formula is available for emerged breakwaters. The increase of R_c reduces $\Delta\overline{\eta}$ in Fig. 4.1. The greater difference between the wave set-up and wave set-down occurs in Tests 3.17 and 3.22 with continuous wave transmission due to the negative value of R_c than in the other tests for the emerged structures with the positive R_c and intermittent wave transmission.

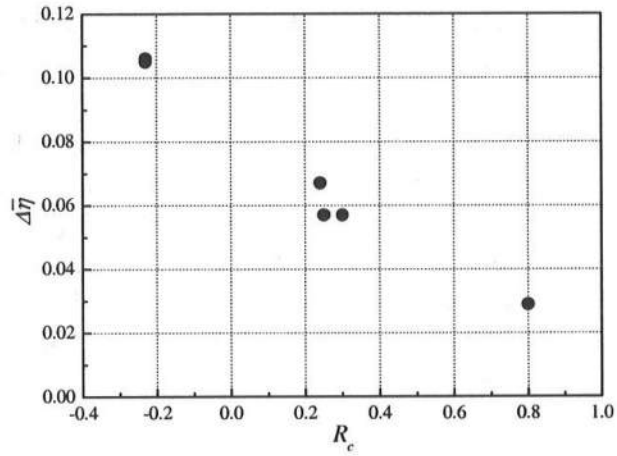

Fig. 4.1 Normalized Mean Water Level Difference $\Delta\overline{\eta}$ as a Function of Normalized Freeboard R_c

In Figs. A.3, the maximum horizontal velocity occurs on the landward (rear) slope of the breakwater due to the large breaking transmitted wave. The minimum horizontal velocity occurs at the seaward (front) slope of the breakwater due to wave downrush before the arrival of the next incident wave. The mean horizontal velocity becomes the largest landward of the highest crest of the structure and the smallest in front of the crest of the front tube. The difference between the maximum and minimum values of the mean velocity $\overline{u}$ is hence the largest for Test 3.32 with the largest R_c and is smaller for Tests 3.17 and 3.22 with R_c<0. In short, Fig. 4.1 depicts the changes of irregular wave breaking, reflection, overtopping and transmission patterns with the increase of the normalized freeboard.

Fig. 4.2 shows the computed spatial variation of the time-averaged volume flux per unit width, $\overline{m} = \overline{hu}$, for Test 3.5. The time averaged continuity equation corresponding to Eq. (3.6) requires $\overline{m} = 0$ (Kobayashi and Wurjanto 1989). The constant volume flux $\overline{m}$ is expected to be

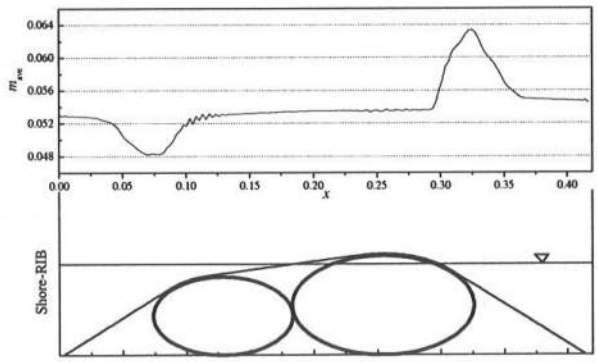

Fig. 4.2 Computed Spatial Variation of Time-Averaged Volume Flux for Test 3.5

positive because the transmission of wave energy accompanies the transmission of water mass over the Shore-RIB structure. Fig. 4.2 indicates numerical errors of the order of 10% of the relatively small constant value of $\overline{m}$.

Figs. A.4(a)-(f) in Appendix show the computed spatial variations of the normalized free surface elevation η above SWL located at z=0 and the normalized depth-averaged horizontal velocity u at the specified normalized time levels for each test. The free surface elevation indicates the wave pattern above the structure. The horizontal velocity indicates the direction of water flow where u>0 landward. The water on the structure flows landward (uprush) and seaward (downrush) on the structure..

The interaction between the wave downrush and incoming wave produces the steep wave front and breaking. For Tests 3.17 and 3.22, incident waves are transmitted over the submerged breakwater with the steep wave front. Incident waves flow over the highly emerged breakwater in Test 3.32.

Table 4.2 Surf Similarity Parameter for Selected 6 Tests

Test	σ	Average $\tan\theta'$	ξ
1.3	15.6	0.87	5.3
2.2	15.2		5.3
3.5	20.2	0.47	3.8
3.17	19.9		3.7
3.22	19.9		3.7
3.32	21.2		4.0

The steep wave front above the seaward slope of the Shore-RIB structure occurs on the gentler slope between the two tubes in Tests 3.5, 3.17, 3.22 and 3.32 rather than on the steep slope of the single tube in Tests 1.3 and 2.2. The steepness of the wave front is related to wave breaking and breaker type. The surf similarity parameter defined as $\xi = \sigma \tan\theta' / \sqrt{2\pi}$ (e.g., Kobayashi et al. 1987) is applied to classify the type of wave breaking where $\tan\theta'$ is the average seaward structure slope between the toe and crest of the structure as calculated by Melby and Resio (2002). Table 4.2 lists the computed surf similarity parameter for each test. The surf similarity parameter ξ~5.3 for the single-tube Shore-RIB in Tests 1.3 and Test 2.2 is greater than ξ~3.8 for the double-tube Shore-RIB in Tests 3.5, 3.17, 3.22 and 3.32. This implies surging waves for ξ~5.3 and collapsing waves for ξ~3.8 if the structure is a uniform slope with no wave overtopping. The present numerical model may not predict the details of wave breaking and flow separation but the computed wave patterns on the structure appear realistic in light of the video observations made by Melby and Resio (2002).

4.4 Wave energy balance

Figs. A.5(a)-(f) in Appendix show the computed spatial variations of the normalized time-averaged wave energy per unit horizontal area, $\overline{E}$, the normalized time-averaged energy flux per unit width, $\overline{E_F}$, and the normalized time-averaged energy dissipation rate per unit horizontal area due to wave breaking, $\overline{D_B}$, above the normalized Shore-RIB structure for each test. Wave energy is the sum of kinetic and potential energy as expressed by Eqs. (3.36a) and (3.36b). In Figs. A.5, there are two peaks in the spatial variation of the time-averaged wave energy for each test. The first

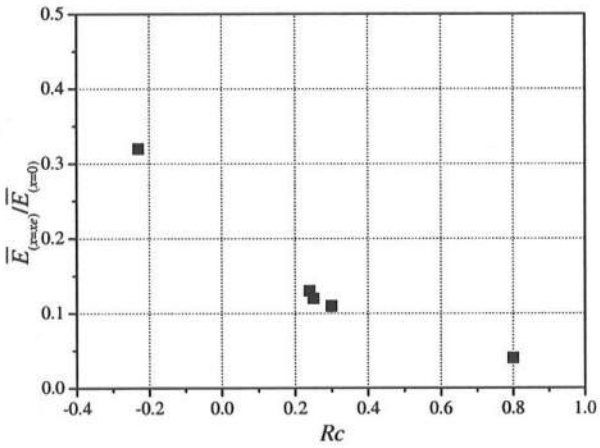

Fig. 4.3 Ratio between Wave Energy $\overline{E}$ at $x=x_e$ and x=0 as a Function of R_c

peak, which is the maximum value in the computation domain, occurs in the vicinity of the landward corner of the front slope of the breakwater. The second peak occurs near the seaward corner of the rear slope of the breakwater. This may result from the changes of the structure slope at these two corners where wave breaking tends to occur. The ratio between $\overline{E}(x=0)$ and $\overline{E}(x=x_e)$ as a function of R_c for each test is shown in Fig. 4.3. $\overline{E}(x=x_e)$ for Tests 3.17 and 3.22 are about 30% of $\overline{E}(x=0)$, whereas $\overline{E}(x=x_e)$ of Test 3.32 is less than 5% of $\overline{E}(x=0)$. As a result, the increase of R_c reduces the landward wave energy as expected.

The wave energy flux per unit width is computed using Eq. (3.37). The time-averaged wave energy flux decreases landward very gradually except near the corners of the slope change as shown in Figs. A.5. The spatial variation of $\overline{E_F}$ determines the energy dissipation rate as expressed in Eq. (3.39). It should be stated that the bottom friction has been neglected by setting $f'=0$ as input as explained in relation to Eq. (3.2).

The time-averaged energy dissipation rate $\overline{D_B}$ is positive or zero. There are two peaks in the spatial variation of $\overline{D_B}$ for each test as shown in Figs. A.5. The landward peak is the maximum for each test. The maximum of $\overline{E}$ and $\overline{D_B}$ occur approximately at the same location. For Tests 1.3 and 2.2, the seaward peak is much smaller than the landward peak because little wave breaking occurred at the seaward corner of the slope change.

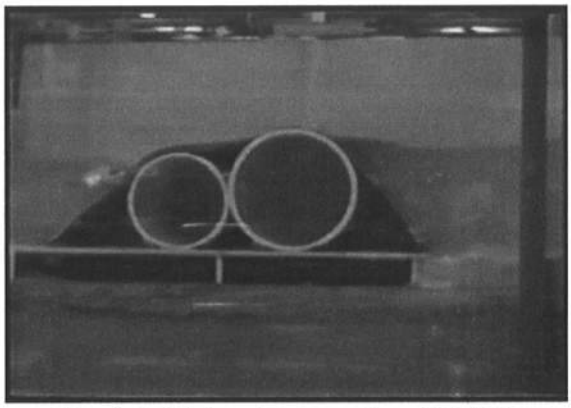

Fig. 4.4(a) Wave Downrush and Bubble Entrainment at Seaward Corner of Slope Change

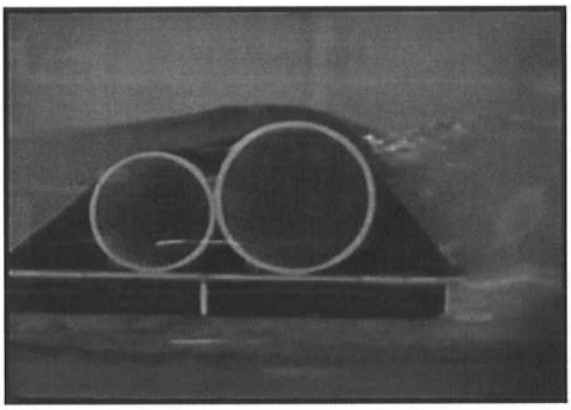

Fig. 4.4(b) Wave Overtopping and Bubble Entrainment at Landward Corner of Slope Change

Possible energy dissipation is examined using the video recording. The seaward corner may cause the initial breaking of incident waves due to the decrease of water depth below the still water level as shown in Fig. 4.4(a). The landward corner may cause the impingement of transmitted waves on the flow from the onshore side as shown in Fig. 4.4(b). It is important to identify the locations where wave breaking occurred and strong eddies were formed above the breakwater. Air bubbles in water may be used to locate the zones of wave breaking and turbulence. Figs. 4.5(a)-(d) show the zones of visible air bubbles obtained from the videotape of the experiment recorded by Melby and Resio (2002). The shaded zones are the zones of frequent air bubbles. The air bubble zones occurred at the landward and seaward corners where the slope changes occurred. For Tests 3.17 and 3.22, incident waves broke on the gentle slope between the two submerged tubes. The bubble zones depicted in Figs. 4.5(a)-(d) are qualitatively consistent with the spatial variations of $\overline{D_B}$ shown in Figs. A.5. However, it should be noted that the numerical model in Chapter 3 does not account for air bubbles.

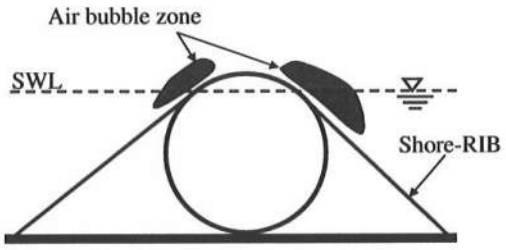

(a) Test 1.3 and 2.2

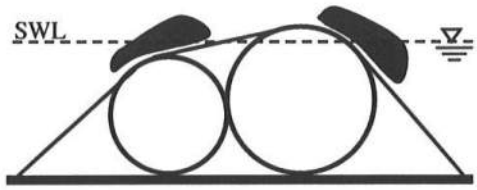

(b) Test 3.5

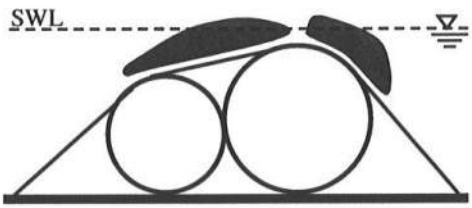

(c) Test 3.17 and 3.22

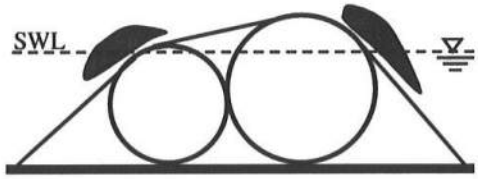

(d) Test 3.32

Figs. 4.5(a)-(d) Air Bubble Entrainment Zones Observed Visually for Each Test

5 WAVE TRANSMISSION COEFFICIENT AND FABRIC TENSION

First, the computed reflection coefficients are presented, and the computed wave transmission coefficients are compared with the measured wave transmission coefficients in Chapter 5.1. To predict the tension acting on the fabric shroud of Shore-RIB, a semi-empirical method is developed in Chapter 5.2. The predicted tension is compared with the measured tension for the three different configurations of the Shore-RIB structure in Chapter 5.3. A design guideline for the fabric shroud is proposed on the basis of the predicted and measured tension in Chapters 5.2 and 5.3.

5.1 Wave Transmission Coefficient and Wave Reflection Coefficient

5.1.1 Wave reflection coefficient

The computed wave reflection coefficients $(K_r)_{mo}$ and $(K_r)_{1/3}$, and the measured and computed wave transmission coefficients $(K_t)_{mo}$ and $(K_t)_{1/3}$ for each of the six tests are shown in Table. 5.1 where the wave reflection coefficient was not measured in the experiment by Melby and Resio (2002) as summarized in Chapter 2.1. $(K_r)_{mo}$ is computed as the ratio of the spectral reflected significant wave height and spectral incident significant wave height and is the same as that given by Eq. (3.28). On the other hand, $(K_r)_{1/3}$ is the ratio of the reflection significant wave height and incident significant wave height based on the average of the highest 1/3 waves. The spectral reflection and transmission coefficients are based on the time-averaged specific wave energy and wave energy fluxes as explained in Chapter 3.2. The other coefficients are based on the significant wave heights.

The computed values $(K_r)_{mo}$ are approximately 0.7 and relatively large for Tests 1.3, 2.2 and 3.32 and are approximately 0.5 for the other tests. The computed reflection coefficients depend on the normalized freeboard R_c and the average slope $\tan\theta'$ listed in Table 4.2. The increase of R_c reduces wave transmission and increases wave reflection for the four tests of Plan 3, which is the two-tube Shore-RIB structure. On the other hand, the average slope $\tan\theta'$, listed in Table.4.2, is larger for the one-tube Shore-RIB structure and the increase of the slope results in larger wave reflection. The trends for $(K_r)_{mo}$ and $(K_r)_{1/3}$ are similar except that $(K_r)_{1/3}$ is slightly smaller than $(K_r)_{mo}$.

Table 5.1 Reflection Coefficients and Transmission Coefficients for Six Tests

Test	$(K_r)_{mo}$	$(K_r)_{1/3}$	$(K_t)_{mo}$		$(K_t)_{1/3}$	
	Computed	Computed	Computed	Measured	Computed	Measured
1.3	0.75	0.68	0.40	0.71	0.59	0.69
2.2	0.75	0.66	0.41	0.50	0.59	0.49
3.5	0.56	0.52	0.34	0.49	0.49	0.46
3.17	0.44	0.41	0.56	0.63	0.64	0.60
3.22	0.44	0.42	0.55	0.60	0.64	0.55
3.32	0.72	0.60	0.23	0.32	0.44	0.29

5.1.2 Wave transmission coefficient

Fig. 5.1 compares the measured and computed wave transmission coefficients $(K_t)_{mo}$ based on the spectral significant wave heights as a function of the normalized freeboard R_c for the tests of Plan 1, 2 and 3 where all the measured values listed in Tables 2.1 and 2.2 are also plotted. $(K_t)_{mo}$ is the ratio between the

spectral transmitted significant wave height and spectral incident significant wave height as defined in Eq. (3.33). The open and solid symbols show the measured and computed values, respectively, where the circle, triangle and square are used for Plan 1, 2 and 3, respectively. The solid line in Fig. 5.1 is the empirical formula for the transmission coefficient of stone-armored breakwaters (D'Angremond et al. 1996)

$$K_t = 0.46 - 0.3\frac{R_c'}{H_{mo}'} = 0.46 - 0.3R_c \quad \text{for stone breakwater} \tag{5.1}$$

The dotted line in Fig. 5.1 is the formula fitted by Melby and Resio (2002) for the data for Plan 3.

$$K_t = 0.53 - 0.28R_c \quad \text{for Plan 3, Shore-RIB} \tag{5.2}$$

The measured and computed values of $(K_t)_{mo}$ decrease linearly with increasing R_c as expressed in Eqs. (5.1) and (5.2). The measured $(K_t)_{mo}$ is slightly larger than that for the stone-armored breakwater probably because of the flexibility of the Shore-RIB structure due to the flexure of the fabric shroud and the lateral excursion of the tube(s) as well as the smooth and impermeable surface of the fabric shroud.

Fig. 5.2 shows the comparison between the measured and computed spectral significant transmission coefficients for the 6 tests. The solid line in Fig. 5.2 corresponds to the perfect agreement. The computed $(K_t)_{mo}$ is smaller than the measured $(K_t)_{mo}$, especially for Plan 1 for which the horizontal tube oscillations were fairly large and may have generated radiated waves. It is noted that the numerical model has not accounted for the structure motion.

Fig. 5.3 shows the measured and computed wave transmission coefficients $(K_t)_{1/3}$ as a function of the normalized freeboard R_c together with the straight lines based on Eq. (5.1). The wave transmission coefficient $(K_t)_{1/3}$ is the ratio between the transmitted significant wave height and incident significant wave height based on the average of the highest 1/3 waves as defined by Eq. (3.34). Both the measured and computed $(K_t)_{1/3}$ are larger than that based on Eq. (5.1) for these 6 tests like $(K_t)_{mo}$ shown in Fig. 5.1. However, the computed $(K_t)_{1/3}$ is slightly larger than the measured $(K_t)_{1/3}$ except for Plan 1 as

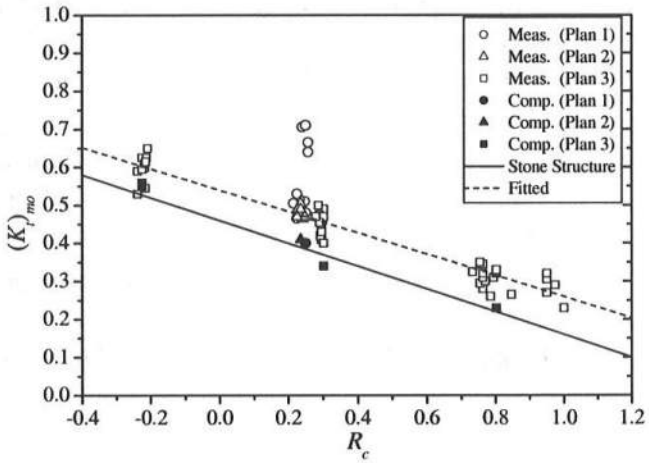

Fig. 5.1 Measured and Computed Wave Transmission Coefficients $(K_t)_{mo}$ vs. R_c

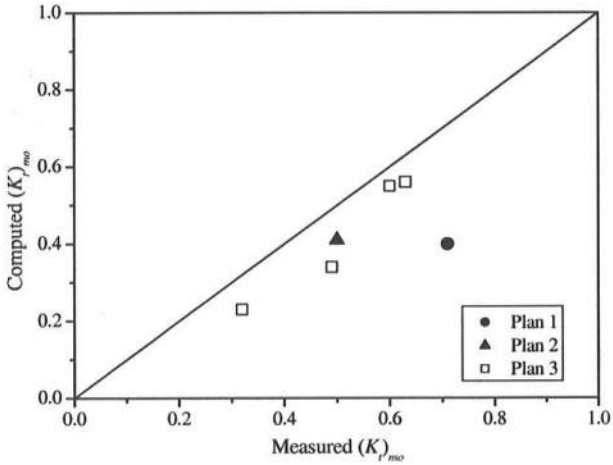

Fig. 5.2 Comparison of Measured and Computed $(K_t)_{mo}$

shown in Fig. 5.4. The difference between the computed $(K_t)_{mo}$ and $(K_t)_{1/3}$ is related to the computed transmitted wave profiles with sharp peaks as shown in Figs. A.1(a)-(f) where the sharp peaks increase the wave heights based on the zero upcrossing method.

Four data points for $(K_t)_{mo}$ for Plan 1 in Fig. 5.1 deviate from the other data points. This is also true for the data point for Plan 1 in Fig. 5.3. This is related to the tube movement for Plan 1 discussed in Chapter 2.2 as well as the fabric shroud static tension T_s' listed in Tables 2.1 and 2.2. Fig. 5.5 shows the measured transmission coefficient $(K_t)_{mo}$ as a function of the normalized static tension $T_s=T_s'/(\rho g H_{mo}'^2)$ for the dimensional freeboard R_c'=-2.7, 2.9 and 7.7 cm for the entire 62 tests. $(K_t)_{mo}$ is essentially independent of T_s for Plan 3 with R_c'=-2.7 and 7.7 cm where R_c'=2.9 cm includes Plans 1, 2 and 3. Several data points for Plans 1 and 2 may be dependent on T_s. The data points for R_c'=2.9 cm for Plans 1 and 2 are selected and shown with the corresponding measured $(K_t)_{mo}$ in Fig. 5.6. Fitted lines of the measured data points for Plans 1 and 2 are plotted in Fig. 5.6 where the dashed line is for Plan 1 and the dotted line is for Plan 2. The measured transmission coefficient $(K_t)_{mo}$ for Plan 1 decreases with increasing T_s when T_s<0.8 and is approximately 0.5 when T_s>0.8. On the other hand, $(K_t)_{mo}$ of Plan 2 is practically independent of T_s. The decreasing trend of $(K_t)_{mo}$ for Plan 1 when T_s<0.8 is associated with the tests with significant tube oscillations caused by no or little pre-tension and no wood chocks as explained in Chapter 2.2. On the other hand, the measured and computed transmission coefficients $(K_t)_{mo}$ are independent of the normalized static tension T_s for the other tests.

5.2 Prediction of Fabric Tension

5.2.1 Horizontal and vertical wave forces

The normalized horizontal wave force $F_h(t)$ and the normalized vertical wave force $F_v(t)$ on the

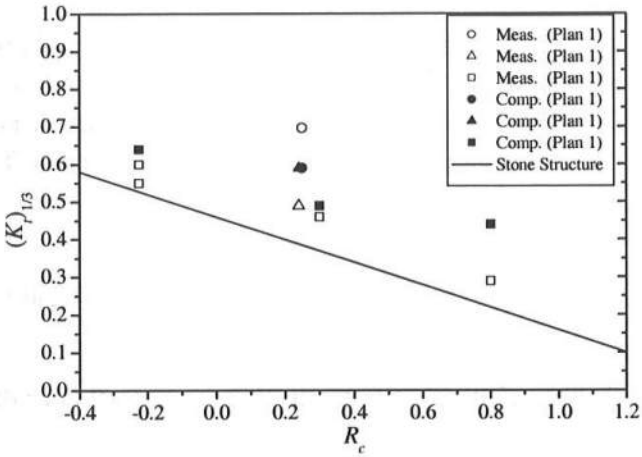

Fig. 5.3 Measured and Computed Wave Transmission Coefficients $(K_t)_{1/3}$ vs. R_c

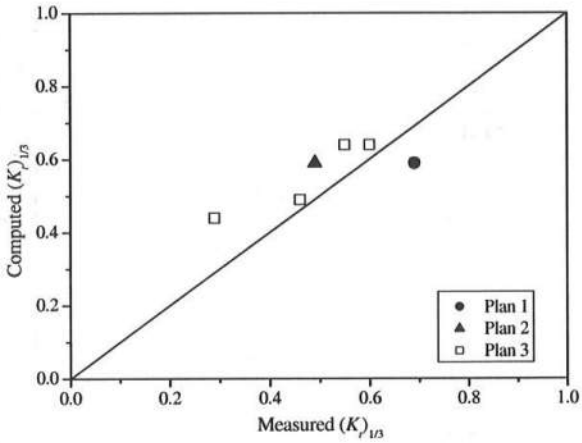

Fig. 5.4 Comparison of Measured and Computed $(K_t)_{1/3}$

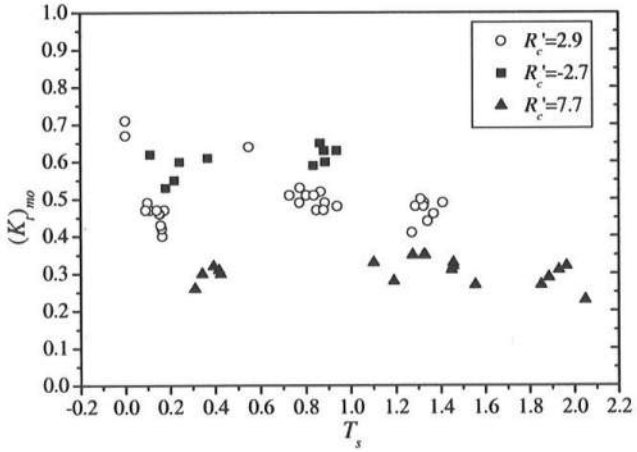

Fig. 5.5 Measured $(K_t)_{mo}$ vs. Normalized Shroud Tension T_s for Freeboard R_c'=-2.7, 2.9 and 7.7 cm

entire breakwater per unit width as a function of the normalized time t are computed for each of the six tests using Eqs. (3.57) and (3.58) in Chapter 3.3. The maximum, mean and minimum values of $F_h(t)$ and $\sigma F_v(t)$ during the total computation duration for each test are obtained and shown in Table 5.2, where σ is the ratio between the horizontal and vertical length scales included in the normalization of the vertical force in Eq. (3.58). The computed F_v turns out to be much smaller than the computed F_h. As a result, the value of σF_v is used in the following where σ is of the order of 20 in Table 5.2. F_h and σF_v are the horizontal and vertical wave forces normalized by $\rho g H_{mo}^{'2}$, respectively.

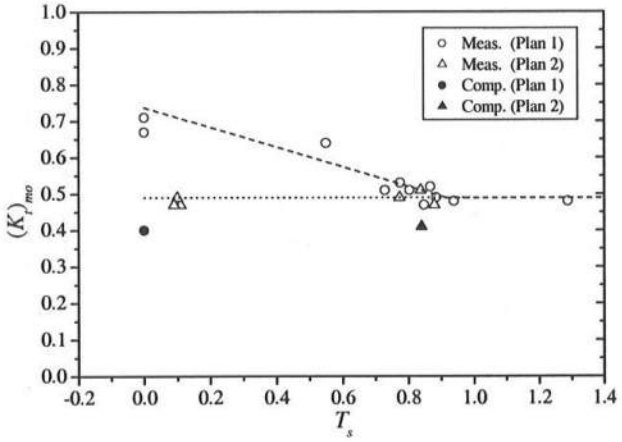

Fig. 5.6 Measured $(K_t)_{mo}$ vs. T_s for Plans 1 and 2

It is very important to estimate the maximum fabric shroud tension of Shore-RIB. The maximum values of the normalized horizontal and vertical wave forces may be related to the maximum fabric shroud tension. As for Plan 3 with the two tubes, the horizontal and vertical wave forces, F_h and σF_v, are the largest for Test 3.32 with the highest normalized freeboard R_c where the values of R_c for the six tests have been listed in Table 4.1.

Table 5.2 Maximum, Mean and Minimum Computed Horizontal and Vertical Wave Forces

Test	F_h			σ	σF_v		
	Max.	Mean	Min.		Max.	Mean	Min.
1.3	3.63	0.00	-2.43	15.6	6.08	0.47	-2.25
2.2	2.96	-0.04	-2.18	15.2	5.36	0.38	-2.13
3.5	3.11	-0.05	-2.23	20.2	5.67	0.75	-3.02
3.17	2.93	-0.20	-2.19	19.9	5.51	-0.12	-3.02
3.22	2.69	-0.20	-2.25	19.9	5.15	-0.12	-3.08
3.32	3.27	0.06	-1.74	21.2	6.74	2.53	0.64

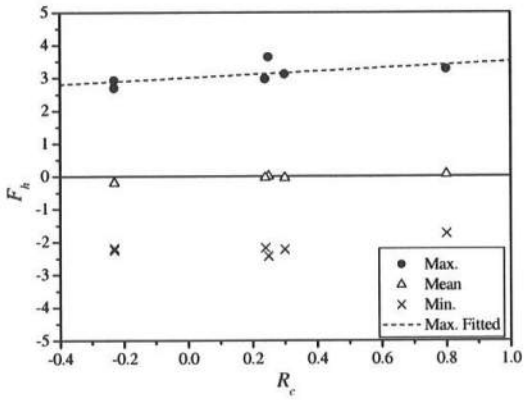

Fig. 5.7 Normalized Horizontal Wave Force F_h vs. Normalized Freeboard R_c

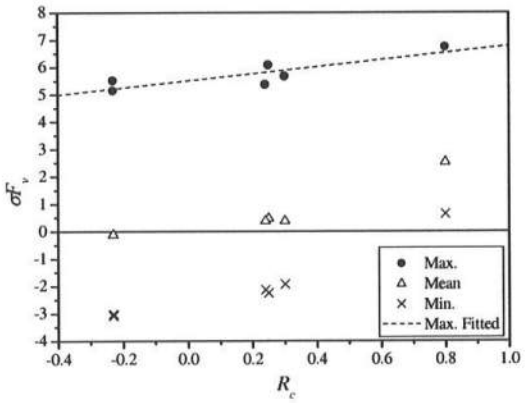

Fig. 5.8 Normalized Vertical Wave Force σF_v vs. Normalized Freeboard R_c

As a result, the maximum horizontal and vertical wave forces may be related to R_c. The maximum, mean and minimum normalized horizontal and vertical wave forces increase somewhat with the increase of the normalized freeboard R_c for the six tests as shown in Figs. 5.7 and 5.8. These fitted straight lines for the maximum F_h and σF_v are expressed as

$$(F_h)_{\max} = 3.0 + 0.5R_c \tag{5.3}$$

$$(\sigma F_v)_{\max} = 5.5 + 1.3R_c \tag{5.4}$$

5.2.2 Measured fabric tension

Figs. 5.9(a) and (b) show the temporal variations of the normalized measured fabric shroud tension per unit width for Test 1.3 with no pre-tension and for Test 3.5 with pre-tension, respectively. The pre-tension on the fabric shroud of Shore-RIB was preloaded before the fabric shroud was exposed to waves as explained in Chapter 2.2. The horizontal axis t expresses the normalized time level, which is the dimensional time level t' divided by the peak period T_p'. The detailed temporal variations for a shorter duration are also shown in these figures. The measured fabric shroud tension per unit width is normalized as $T=T'/\rho g H_{mo}'^2$, where T' is the dimensional fabric shroud tension measured using two load cells as explained in Chapter 2.1. The measured fabric tension varied in complicated manners. In addition, low frequency oscillations with normalized wave periods much larger than unity are visible in the temporal variations of the fabric tension $T(t)$. This may result from various causes such as wave groups and tubes oscillating intermittently with unknown friction forces between the tube and the fabric shroud and bottom. As a result, it is difficult to predict the temporal variations of the fabric tension accurately. Instead, the maximum fabric shroud tension is estimated using the computed wave force in the following.

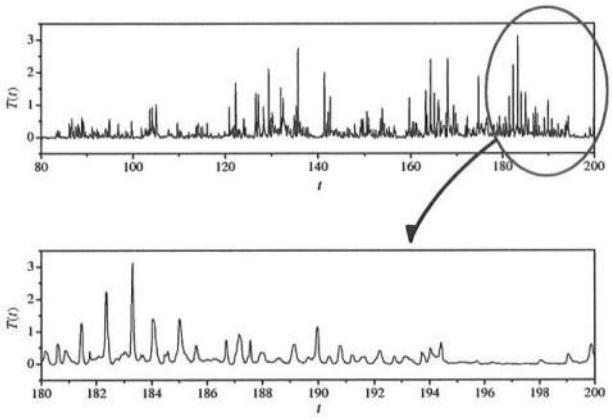

Fig. 5.9(a) Measured Normalized Fabric Tension for Test 1.3

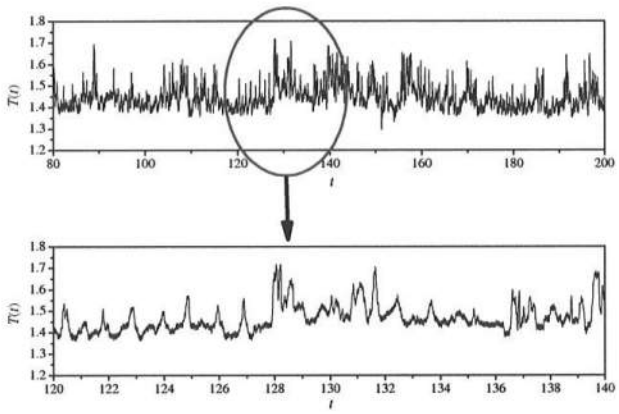

Fig. 5.9(b) Measured Normalized Fabric Tension for Test 3.5

5.2.3 Semi-empirical prediction method

As shown in Figs. 5.9(a) and (b), the normalized measured fabric tension $T(t)$ is positive even for Test 1.3 with no pre-tension. If the fabric shroud of Shore-RIB had behaved like an elastic spring, the temporal

variation of $T(t)$ should have oscillated about the normalized pre-tension T_s, in which $T_s = T_s'/\rho g H_{mo}'^2$ where T_s'=dimensional pre-tension in the absence of waves. However, the temporal variation of $T(t)$ did not become smaller than T_s. This is because the fabric is not elastic and appears to respond to the wave-induced positive tension only.

The normalized fabric tension $T(t)$ may hence be separated into the pre-tension T_s and the wave-induced normalized tension $T_w(t)$

$$T(t) = T_s + T_w(t) \tag{5.5}$$

where $T_w(t)$=time-varying fabric tension which is positive or zero. On the other hand, the computed horizontal and vertical wave forces, $F_h(t)$ and $F_v(t)$, oscillate about zero. It is now necessary to relate the computed wave force to the measured fabric tension in order to estimate the actual fabric tension acting on the fabric shroud of Shore-RIB.

The horizontal wave force F_h and the vertical wave force F_v act on the Shore-RIB structure dynamically together with the other forces as illustrated in Fig. 3.4. The horizontal and vertical wave forces may be transmitted to the fabric shroud and the tube. The tube(s) can oscillate in the cross-shore direction and the tube oscillation may cause additional fabric tension, even if the tube oscillation is reduced significantly by the wood chocks for Plans 2 and 3 as shown in Figs. 2.4 and 2.5. On the other hand, the tube(s) did not move in the vertical direction. Hence, the vertical wave force F_v may be assumed to be transmitted to the tube and then to the bottom without causing much tension in the fabric. Meanwhile, the horizontal wave force causes the lateral force on the tube(s) and an additional tension force in the fabric. As a result, the computed horizontal wave force is used to estimate the measured fabric tension.

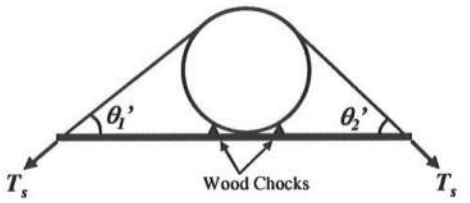

Fig. 5.10(a) Static Force Balance in Absence of Waves (F_h=0)

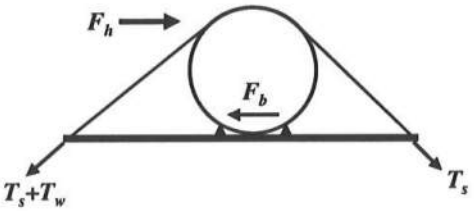

Fig. 5.10(b) Quasi Static Force Balance for Landward Wave Force (F_h>0)

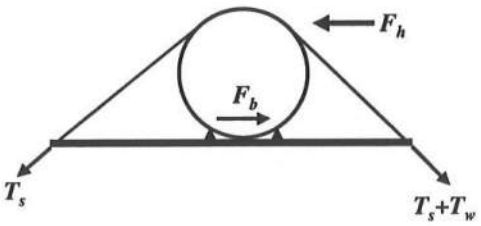

Fig. 5.10(c) Quasi Static Force Balance for Seaward Wave Force (F_h<0)

Figs. 5.10(a), (b) and (c) show the force balance on the Shore-RIB structure for the three cases corresponding to the horizontal wave force F_h=0, F_h>0 and F_h<0. Fig. 5.10(a) is the case of no wave action with F_h=0 where the static tension T_s is constant in the absence of friction between the fabric shroud and tube(s). Denoting θ_1' = angle between the seaward fabric shroud and horizontal plane and θ_2' = angle between the landward fabric shroud and horizontal plane, the static horizontal force balance requires $\theta_1' = \theta_2'$ and use is made of $\theta' = \theta_1' = \theta_2'$ for simplicity where $\theta' = \theta_1' = \theta_2' = 43.5^o$ for Plans 1 and 2 and $\theta' = \theta_1' = \theta_2' = 47.1^o$ for Plan 3 where the above value of θ' used hereafter is different from θ' used for the average slope $\tan\theta'$ in Table 4.2

When the incoming wave crest acts on the front (seaward) slope of the Shore-RIB structure with no wave crest landward of the crest of Shore-RIB, the total horizontal wave force acts in the landward direction and F_h>0 as shown in Fig.

5.10(b). After the overtopping wave crest propagates landward of the Shore-RIB crest with wave downrush on the front (seaward) slope of the Shore-RIB, the total horizontal wave force acts in the seaward direction and $F_h<0$ as shown in Fig. 5.10(c). The horizontal force F_b which prevents or reduces the tube shifting in the cross-shore direction acts mainly between the bottom of the tube(s) and the attached wood chocks as depicted in Figs. 5.10(b) and (c) where the wave-induced fabric tension T_w is assumed to occur on the tension side of the fabric shroud against the wave-induced force F_h. Since the fabric tension $T(t)$ was measured only on the seaward side of the fabric shroud, the following analysis of the wave-induced tension $T_w(t)$ is limited to the case $F_h>0$. The wave-induced tension $T_w(t)$ acting for the case $F_h<0$ is not analyzed but may be less than T_w for the case of $F_h>0$ because the landward wave force is computed to be larger than the seaward wave force as presented in Table 5.2.

The wave-induced tension $T_w(t)$ on the seaward side of the fabric shroud may thus be estimated as

$$T_w(t)\cos\theta' = F_h(t) - F_b(t) \quad \text{for } F_h > 0 \tag{5.6a}$$

$$T_w(t) = 0 \quad \text{for } F_h \le 0 \tag{5.6b}$$

which is based on the quasi-static horizontal force balance. $F_b(t)$ varying temporally against $F_h(t)$ is difficult to estimate because the contact problem between the tube(s) and the bottom is difficult to formulate. $F_b(t)$ is likely to be affected by the fabric pre-tension T_s and the wood chocks which controlled the degree of the tube(s) oscillation and rolling as explained before. As a result, a semi-empirical approach is adopted in the following.

The measured maximum wave-induced tension, $(T_w)_{max}=T_{max}-T_s$, using Eq. (5.5) is obtained from the measured maximum tension T_{max} and the static tension T_s listed in Tables 2.1 and 2.2 for each of the 62 tests where the normalized tension is the dimensional tension divided by $\rho g H_{mo}'^2$ for each test. Fig. 5.11 shows $(T_w)_{max}$ as a function of T_s for the 62 tests. For Plan 1, there was no wood chock attached to the Shore-RIB structure as shown in Fig. 2.3. The wood chocks were attached to the Shore-RIB structure for Plans 2 and 3 as shown in Figs. 2.4 and 2.5. Plan 2 was the single-tube Shore-RIB structure with two wood chocks attached to the one tube. Four wood chocks were attached for the case of Plan 3 with the two-tube Shore-RIB structure. Fig. 5.11 indicates that $(T_w)_{max}$ decreases clearly with increasing T_s and the increase of the number of wood chocks from Plan 1 to Plan 2 and then from Plan 2 to Plan 3.

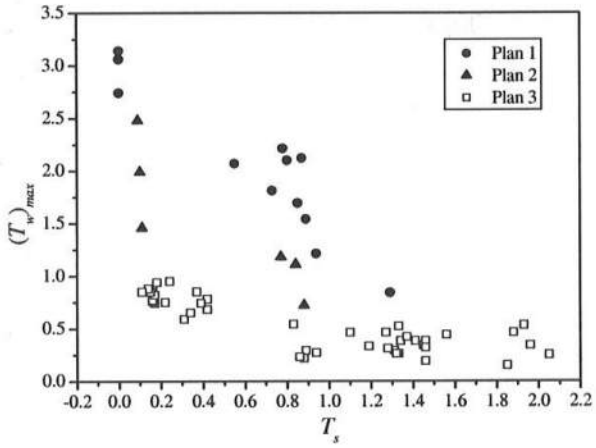

Fig. 5.11 Measured $(T_w)_{max}$ vs. Measured T_s for 62 Tests.

As a result, an empirical reduction factor r is introduced to approximate the right hand side of Eq. (5.6a) as

$$F_h(t) - F_b(t) = r\,F_h(t) \quad \text{for } F_h > 0 \tag{5.7}$$

where r= reduction factor ($0<r\le1$) due to the static pre-tension T_s and the number of wood chocks. The

value of r is assumed to be independent of time t.

Substitution of Eq. (5.7) into Eqs. (5.6a) and (5.6b) yields

$$T_w(t) = \frac{r}{\cos\theta'} F_h(t) \qquad \text{for } F_h>0 \tag{5.8a}$$

$$T_w(t) = 0 \qquad \text{for } F_h\leq 0 \tag{5.8b}$$

Using Eq.(5.5), Eq.(5.8a) is expressed as

$$T(t) - T_s = \frac{r}{\cos\theta'} F_h(t) \quad \text{for } F_h>0 \tag{5.9}$$

which yields the maximum tension T_{max} as a function of the maximum horizontal wave force $(F_h)_{max}$

$$T_{\max} - T_s = \frac{r}{\cos\theta'} (F_h)_{\max} \tag{5.10}$$

It should be noted that the fabric tension and horizontal wave force per unit width have been normalized using the value of $\rho g H_{mo}'^2$ for each test.

To develop an empirical formula for r, Eq. (5.10) is rewritten as

$$r = \frac{(T_{\max} - T_s)\cos\theta'}{(F_h)_{\max}} \tag{5.11}$$

which implies that the value of r is estimated using the maximum values of T and F_h. Substitution of Eq. (5.3) into Eq. (5.11) with $(T_w)_{max}=(T_{max} - T_s)$ yields

$$r = \frac{(T_w)_{\max}\cos\theta'}{3.0+0.5R_c} \qquad ; \qquad (T_w)_{\max} = T_{\max} - T_s \tag{5.12}$$

where $R_c=R_c/H_{mo}'$ is the normalized freeboard. The reduction factor r can be calculated using the measured quantities T_{max}, T_s, $\cos\theta'$ and R_c for each of the 62 tests. Fig. 5.12 shows the calculated reduction factor r as a function of the pre-tension T_s in a manner similar to Fig. 5.11. All the values of r are in the range $0<r\leq 1$ as expected. The fitted straight lines plotted for Plans 1, 2 and 3 are expressed as

$$r_1 = 0.7 - 0.35T_s \qquad \text{for Plan 1} \tag{5.13}$$

$$r_2 = 0.5 - 0.32T_s \qquad \text{for Plan 2} \tag{5.14}$$

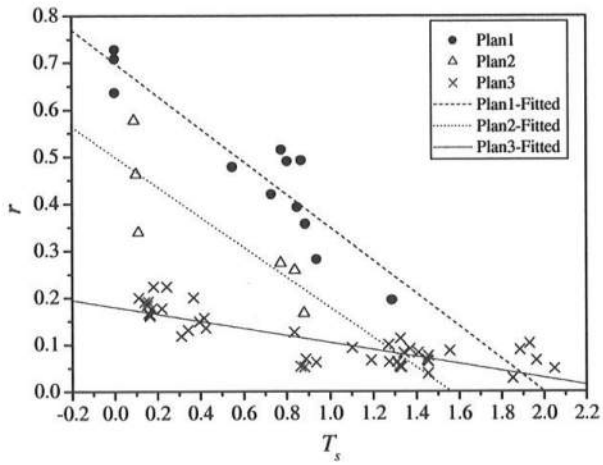

Fig. 5.12 Reduction Factor r as Function of T_s

$$r_3 = 0.18 - 0.075T_s \quad \text{for Plan 3} \tag{5.15}$$

where r_i with $i = 1, 2$ and 3 corresponds to Plan i.

To assess the accuracy of these empirical equations, the maximum fabric tension T_{max} is predicted empirically using Eq. (5.12) as

$$(T_{\max})_{predicted} = T_s + \frac{r_i(T_s)}{\cos\theta'}(3.0 + 0.5R_c) \tag{5.16}$$

Fig. 5.13 shows the comparison between the measured maximum tension $(T_{max})_{measured}$ and the predicted maximum tension $(T_{max})_{predicted}$ based on Eq. (5.16) for each of the 62 tests. The comparison of Figs. 5.12 and 5.13 indicates that the scatter of data points used to develop the empirical equations (5.13)-(5.15) is reduced when these equations are used to estimate T_{max}. This implies that the errors associated with Eqs. (5.13)-(5.15) are reduced in the estimation of T_{max}.

The true test of Eqs. (5.13)-(5.15) lies in whether the time-invariant value of r can predict the time-varying fabric tension $T_w(t)$ from the computed horizontal wave force $F_h(t)$ using Eqs. (5.9) and (5.8b).

$$T(t) = T_s + \frac{r_i(T_s)}{\cos\theta'}F_h(t) \qquad \text{for } F_h > 0 \tag{5.17}$$

$$T(t) = T_s \qquad \text{for } F_h \le 0 \tag{5.18}$$

where the values of T_s and $\cos\theta'$ are known for each test and r_i for Plan i is given by Eq. (5.13), (5.14) or (5.15). It should be noted that these equations may yield good agreement for T_{max} as shown in Fig. 5.13 but may not be accurate enough to predict the detailed temporal variation of the measured tension $T(t)$.

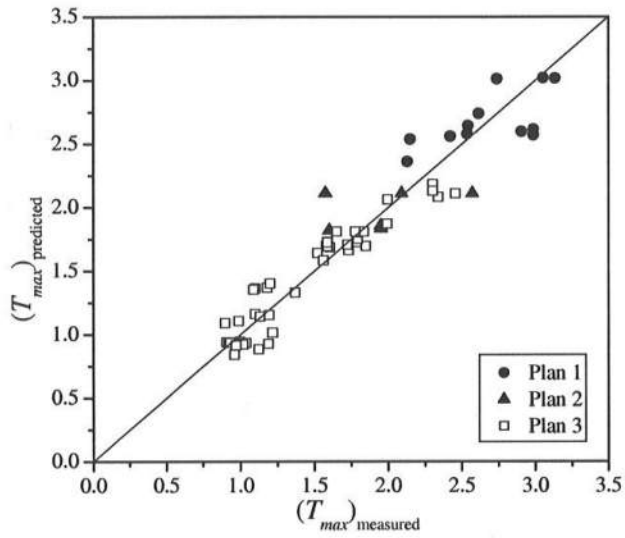

Fig. 5.13 Comparison between Measured and Predicted Maximum Tension T_{max}

5.3 Measured and Predicted Temporal Variations of Fabric Tension

The fabric tension $T(t)$ is calculated using Eqs. (5.17) and (5.18) with the computed horizontal wave force $F_h(t)$ for each of the selected six tests. Figs. B.1(a)-(f) in Appendix show the normalized time series of the measured tension and predicted tension as a function of the normalized time t for each test. It is clear that the present numerical model cannot predict the detailed temporal variation of the tension affected by the complicated tube oscillations which are neglected in the present model. Low frequency oscillations are apparent in the temporal variation of the measured tension. The lower bound of the predicted tension is limited by the pre-tension T_s during the computation duration. At least the present model predicts the range $T_s \le T(t) \le T_{max}$ fairly well.

For Test 1.3, the largest peak occurs at the normalized time $t \sim 184$ in the measured temporal variation. A large peak also occurs at the approximately same time in the predicted temporal variation. Some of the

other peaks in the measured and predicted tensions appear synchronously. On the other hand, the disagreement is large during $120<t<200$ with large peaks and $40<t<120$ with sparse small peaks in the measured temporal variation. Relatively large peaks occur continuously during the entire computation duration in the predicted temporal variation. In short, the present model is not accurate for Test 1.3 with significant tube oscillations.

For Tests 2.2 and 3.32, only a few groups of peaks are visible in the measured temporal variation at t~25 for Test 2.2 at t~45 and 143 for Test 3.32. Some peaks in the predicted temporal variation occur at the approximately same time for Test 2.2. No correlation between the measured and predicted temporal variations exists for Test 3.32.

Better agreement between the measured and predicted temporal variations is obtained for Tests 3.5, 3.17 and 3.22. For Test 3.17, several groups of large peaks in the measured tension appear at the approximate same time in the predicted tension. However, the predicted tension exhibits more frequent and larger peaks than the measured tension. The agreement between the measured and predicted temporal variations is relatively better for Tests 3.5 and 3.22.

In summary, the strong irregularity of the temporal variation of the measured tension makes it difficult to predict the detailed temporal variation of the fabric tension. However, the range of the temporal variation is predicted well by the present model based on the measured T_s and the empirical equations for the reduction factor r obtained from the measured T_{max}. For the design of the fabric shroud, it is safer to reduce the range $T_s \le T(t) \le T_{max}$ because of the uncertainty of the predicted temporal variation.

Figs. B.2(a)-(f) in Appendix compare the power spectra of the normalized measured and predicted tension for each test. These normalized spectra are plotted as a function of the normalized frequency $f = f' T_p'$ with f'=dimensional frequency. The power spectra of the measured tension in the low frequency range f~0 are dominant for each test especially for Test 3.22. The power spectra of the predicted tension are much smaller in the low frequency range f ~0 but show the peak at f=1, corresponding to the peak of the incident wave spectrum. This indicates that the measured fabric tension was not induced by individual waves in the incident wave train.

Table 5.3 shows the mean and standard deviation of the measured and predicted tension together with the normalized measured pre-tension T_s for each test. The error (%) is based on the absolute difference between the measured and predicted mean tension divided by the measured tension. The agreement between the measured and predicted tension is good for Tests 3.5, 3.17 and 3.32. Large errors occur for Tests 1.3 and 3.22 because of the small pre-tension T_s of the fabric shroud for Tests 1.3 and 3.22. The agreement is worse for Test 2.2 than for Tests 3.5, 3.17 and 3.32 for the two-tube Shore-RIB structure probably because the single tube moved more than the two tubes for the similar pre-tension T_s. Table 5.3 confirms better agreement for the tests with the narrow range of $T_s \le T(t) \le T_{max}$ where T_{max} is generally smaller for Plan 3 with the two tubes as shown in Fig. 5.13.

Table 5.3 Mean and Standard Deviation of Measured and Predicted Tension

Test	Pre-Tension T_s	Mean			Standard Deviation	
		Measured	Predicted	Error (%)	Measured	Predicted
1.3	0.00	0.15	0.35	133.3	0.24	0.52
2.2	0.84	1.05	0.94	10.5	0.12	0.16
3.5	1.41	1.46	1.44	1.4	0.06	0.05
3.17	0.94	1.02	0.97	4.9	0.03	0.06
3.22	0.24	0.46	0.28	39.1	0.14	0.08
3.32	1.46	1.50	1.49	0.7	0.04	0.06

Fig. 5.14 shows the comparison between the measured and predicted mean tension for the six tests. The solid line in Fig.5.14 corresponds to the perfect agreement. This confirms better agreement for the tests with the large T_s and mean tension. Fig. 5.15 shows the standard deviations of the measured and predicted tension as a function of the pre-tension T_s for the six tests. The increase of T_s reduces the reduction factor r as shown in Fig. 5.12 and the corresponding maximum tension T_{max} in Eq. (5.16). As a result, the increase of T_s results in the reduced range $T_s \leq T(t) \leq T_{max}$ with the smaller standard deviation.

This confirms the suggested design guideline for the fabric shroud based on the reduced difference between T_{max} and T_s where T_{max} can be estimated using Eq. (5.16) with Eqs. (5.13)-(5.15).

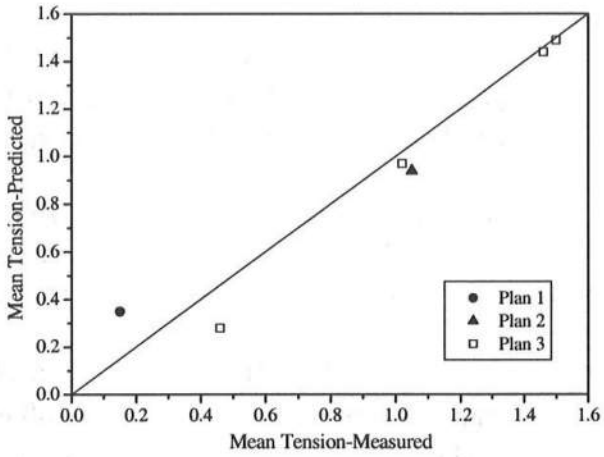

Fig. 5.14 Correlation between Measured and Predicted Mean Tension

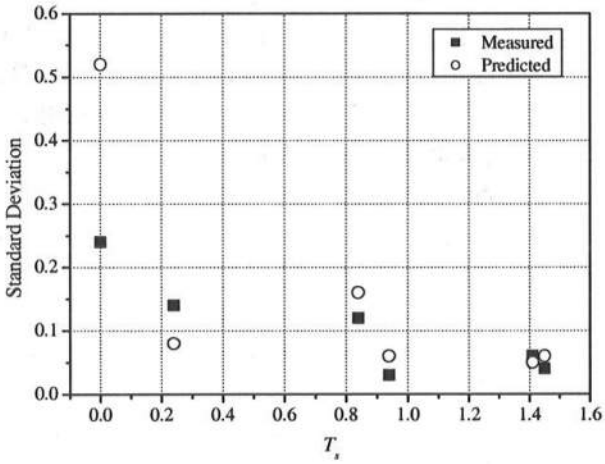

Fig. 5.15 Standard Deviation of Tension vs. Pre-Tension T_s

6 SUMMARY AND CONCLUSIONS

The numerical model is developed to predict irregular wave breaking and transmission as well as wave force on submerged and emerged impermeable structures. The developed numerical model is compared with available laboratory data on a nearshore rapidly-installed breakwater (Shore-RIB) consisting of one or two tubes held by an anchored fabric shroud. A small-scale physical model study conducted by Melby and Resio (2002) investigated the functional and structural response of the Shore-RIB structure model including the wave transmission coefficient K_t and the fabric shroud tension $T(t)$ as a function of time t for 62 tests.

The present numerical model based on finite-amplitude, shallow-water waves over rigid and impermeable structures is not capable of predicting the detail responses of Shore-RIB. The computed transmitted wave train exhibits sharp peaks of intermittently overtopping waves. The present numerical model, however, cannot predict the development of an undular bore landward of Shore-RIB since wave dispersion is not accounted for. The power spectra of the measured transmitted free surface elevation η_t in the low frequency range are found to be relatively large because groups of large waves overtop the structure together and the intermittent tube oscillation in the cross-shore direction may have generated waves. The computed normalized mean water level difference $\Delta\bar{\eta}$ due to wave set-up and wave set-down decreases with the increase of the normalized freeboard R_c for the range $-0.3 < R_c \leq 0.8$ where positive R_c implies an emerged Shore-RIB.

The computed spatial variation of the time-averaged wave energy dissipation rate $\overline{D_B}$ is consistent with the video recording of the locations of wave overtopping and impingement as well as the interaction of wave downrush and incoming wave. There are two peaks in the spatial variation of $\overline{D_B}$. Both peaks occur in the vicinities of the seaward and landward corners of the structure where wave breaking tends to occur. Wave breaking at the front corner of the structure is more intense for the two-tube model than the single-tube model and this trend also appears in the spatial variations of the computed $\overline{D_B}$.

The measured transmission coefficient $(K_t)_{mo}$ is slightly larger than that predicted by the empirical formula for stone-armored breakwaters (D'Angremond et al. 1996) because of the flexibility of the Shore-RIB structure due to the flexure of the fabric shroud and the lateral excursion of the tube as well as the smooth and impermeable surface of the fabric shroud. Meanwhile, the computed $(K_t)_{mo}$ is slightly smaller than the measured $(K_t)_{mo}$ since the numerical model assumes a rigid structure. Both measured and computed transmission coefficients $(K_t)_{mo}$ decrease linearly with the increase of the normalized freeboard R_c of the Shore-RIB structure.

The measured transmission coefficient $(K_t)_{mo}$ for Plan 1, corresponding to the single-tube model with small static pre-tension and no wood chocks, decreases with the increase of the normalized static tension T_s when T_s<0.8, whereas $(K_t)_{mo}$ for the other tests are practically independent of T_s. The decreasing trend of $(K_t)_{mo}$ for Plan 1 when T_s<0.8 is associated with the tests with significant tube oscillations caused by no or little pre-tension and no wood chocks used for preventing tube movement in the cross-shore direction. On the other hand, the measured and computed transmission coefficients $(K_t)_{mo}$ are independent of the normalized static tension T_s for the other tests.

The maximum, mean and minimum normalized computed horizontal wave forces increase somewhat with the increase of the normalized freeboard R_c and a linear regression analysis for the maximum force $(F_h)_{\max}$ yields $(F_h)_{\max} = 3.0 + 0.5R_c$. The maximum fabric tension is predicted semi-empirically using (a) the predicted horizontal wave force $(F_h)_{max}$; (b) the empirical reduction factor r, which is dependent on pre-tension T_s and the number of wood chocks; and (c) the static pre-tension T_s. The predicted maximum

fabric tension T_{max} is shown to be fairly accurate for the three different configurations (Plans 1, 2 and 3). It should be noted that the present numerical model cannot predict the detailed temporal variation of the fabric tension because the fabric tension is affected by the complicated tube oscillations that are neglected in the present model. However, the present numerical model predicts the measured range $T_s \leq T(t) \leq T_{max}$ of the oscillatory tension force $T(t)$ fairly well.

The flexibility of the fabric shroud and the excursion of the single tube increased the fabric tension when the tube was not constrained by wood chocks and sufficient fabric pre-tension T_s. The two-tube configuration with two wood chocks for each tube reduced the tube oscillations and temporal variation of the fabric tension considerably. It is recommended to reduce the temporal range between T_s and the maximum tension T_{max} predicted by the simple semi-empirical method so as to minimize the uncertain temporal fluctuations of the fabric tension that may eventually cause fatigue damage to the anchored fabric shroud.

REFERENCES

Broderick, L.L., and Leonard, J.W. (1995) : Nonlinear response of membranes to ocean waves using boundary and finite elements, Ocean Engineering, 7, pp.731-745.

Cho, I.H., Kee, S.T. and Kim, M.H. (1997) : The performance of flexible-membrane wave barriers in oblique incident waves," Applied Ocean Research, 19, pp.171-182.

D'Angremond, K., Van der Meer, J.W., De Jong, R.J. (1996) : Wave transmission at low-crested structures," Proc. 25th Coastal Engineering Conference, ASCE, pp.2418-2427.

Dewi, F.D.H., Liapis, S.I., and Plaut, R.H. (1999) : Three-dimensional analysis of wave attenuation by a submerged horizontal, bottom-mounted, flexible shell, Ocean Engineering, 26(9), pp.813-839.

Kobayashi, N. (1999) : Future of coastal engineering and structures, Proc. Coastal Structures'99, Balkema, pp.1147-1154.

Kobayashi, N., Otta, A.K., and Roy, I. (1987) : Wave reflection and run-up on rough slopes, Journal of Waterway, Port, Coastal, and Ocean Engineering, ASCE, 113 (3), pp.282-298.

Kobayashi, N., and Raichle, A.W. (1994) : Irregular wave overtopping of revetments in surf zones, Journal of Waterway, Port, Coastal, and Ocean Engineering, ASCE, 120 (1), pp.56-73.

Kobayashi, N., and Wurjanto, A. (1989) : Wave transmission over submerged breakwaters, Journal of Waterway, Port, Coastal, and Ocean Engineering, ASCE, 115 (5), pp.662-680.

Kobayashi, N., and Wurjanto, A. (1992) : Irregular wave setup and run-up on beaches, Journal of Waterway, Port, Coastal, and Ocean Engineering, ASCE, 118 (4), pp.368-386.

Liapis, S.I., Constantine, L.S., and Trowbridge, J.D. (1996) : On the use of flexible structure as a breakwater, Offshore Mechanics and Arctic Engineering, Chakrabarti, S., et al. (Eds), Vol I, Part B, ASME, pp.41-47.

Melby, J.A. and Resio, D.T. (2002) : A nearshore rapidly-installed breakwater, Proc. 28th Coastal Engineering Conference, ASCE (in press).

Milgram, J.H. (1971) : Forces and motions of a flexible floating barrier, Journal of Hydronautics, 5(2), pp.41-51.

Ohyama, T., Tanaka, M., Kiyokawa, T., Uda, T., and Murai, Y. (1989) : Transmission and reflection characteristics of waves over a submerged flexible mound, Coastal Engineering in Japan, 32, pp.53-68.

Ohyama, T., Tsuchida, M. and Nadaoka, K. (2000) : Modeling the floating-body motion in nonlinear random waves based on vertically integrated wave equations, Applied Ocean Research, 22,

pp.155-167.
Peregrine, D.H. (1966) : Calculations of the development of an undular bore, Journal of Fluid Mechanics, 25(2), pp.321-330.
Phadke, A.C. and Cheung, K.F. (1999) : Response of bottom-mounted fluid-filled membrane in gravity waves, Journal of Waterway, Port, Coastal, and Ocean Engineering, ASCE, 125(6), pp.294-303.
Sawaragi, T., Aoki, S. and Liu, H. (1989) : Wave deformation and forces on a submerged silt curtain, Proc. 30th Japanese Conference on Coastal Engineering, JSCE, 36, pp.559-563. (in Japanese)
Seabrook, S.R., and Hall, K.H. (1998) : Wave transmission at submerged rubblemound breakwaters, Proc. 26th Coastal Engineering Conference, ASCE, pp.2000-2013.
Van der Meer, J.W., Regeling, E. and De Waal, J.P. (2000) : Wave transmission: spectral changes and its effects on run-up and overtopping, Proc. 27th Coastal Engineering Conference, ASCE, pp.2156-2168.

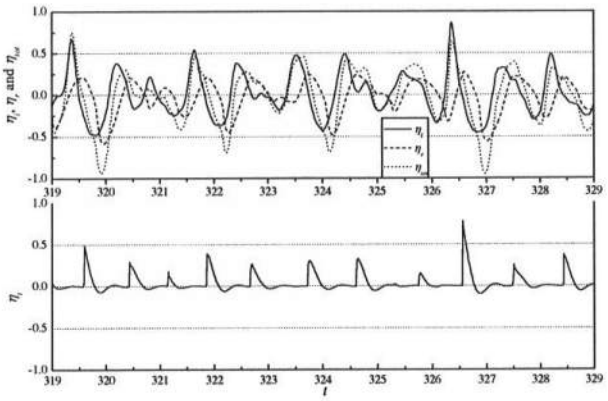

(a) Test 1.3

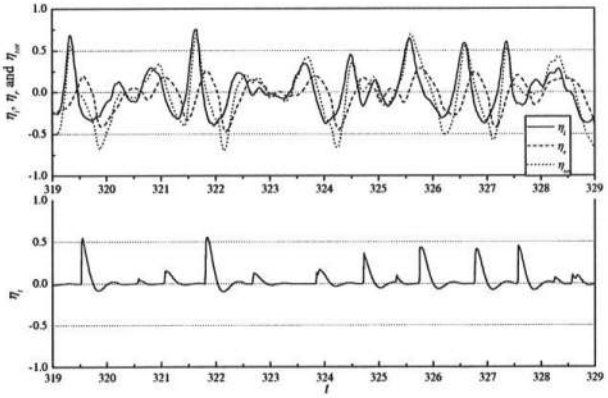

(b) Test 2.2

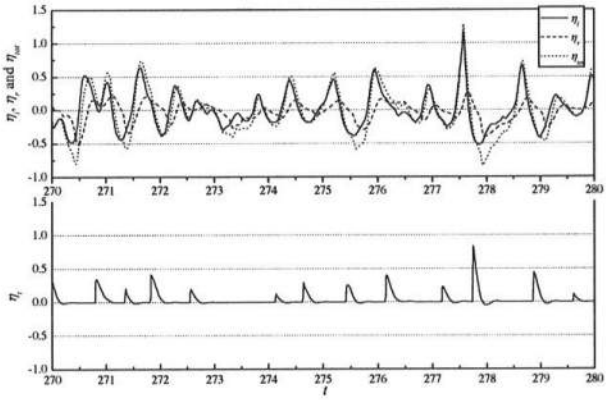

(c) Test 3.5

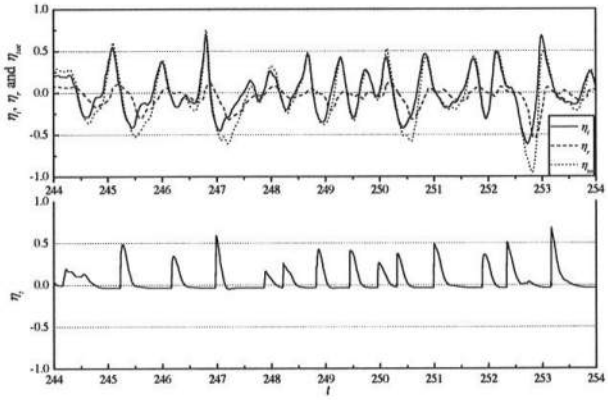

(d) Test 3.17

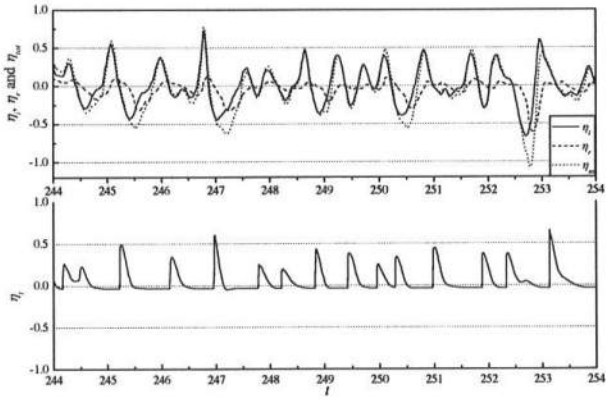

(e) Test 3.22

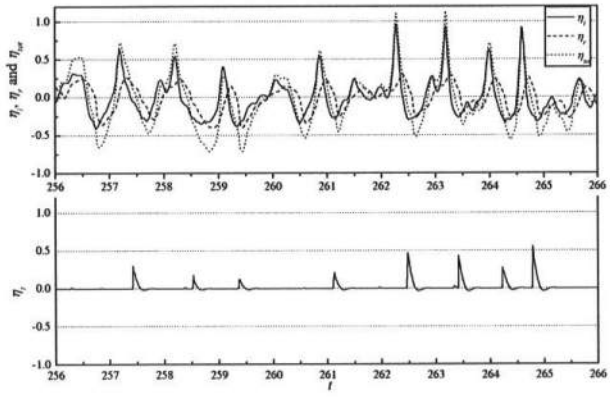

(f) Test 3.32

Figs. A.1(a)-(f) Computed Time Series of Free Surface Elevation at Seaward and Landward Boundaries

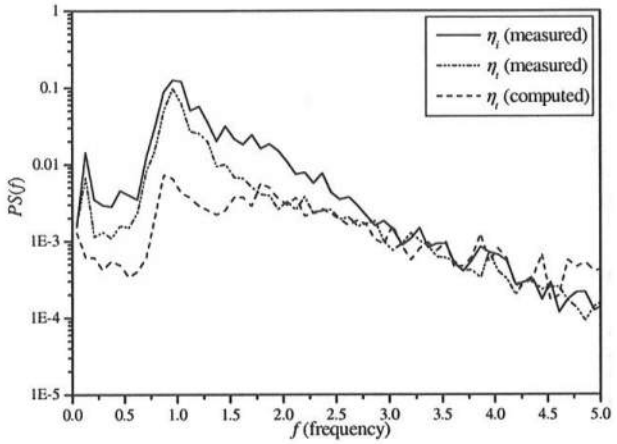

(a) Test 1.3

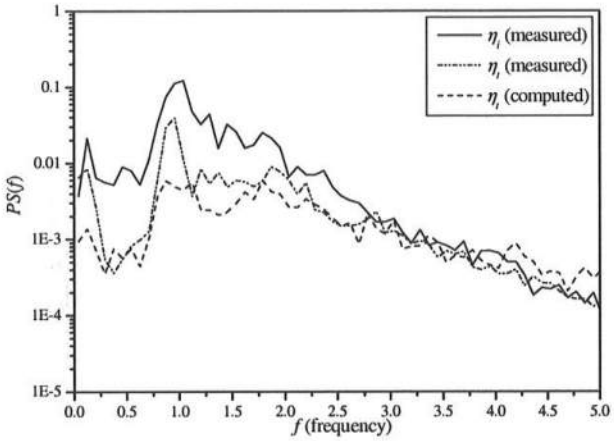

(b) Test 2.2

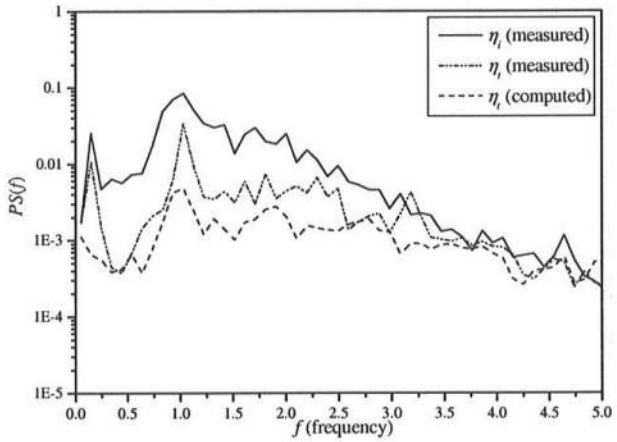

(c) Test 3.5

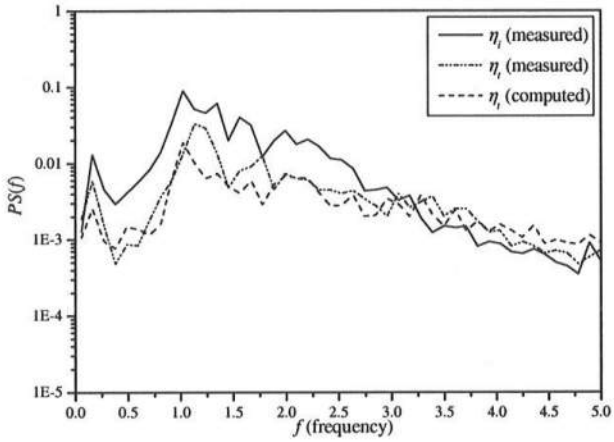

(d) Test 3.17

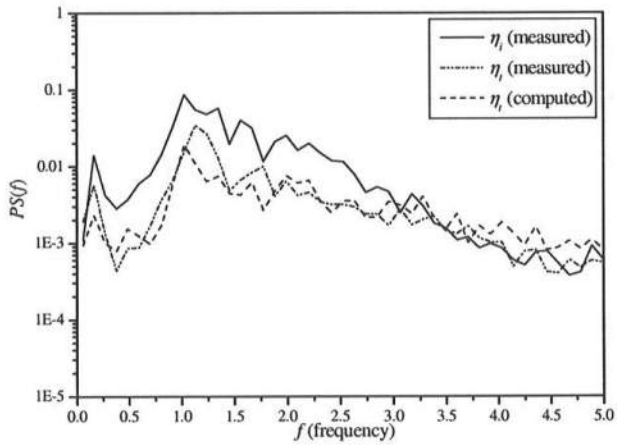

(e) Test 3.22

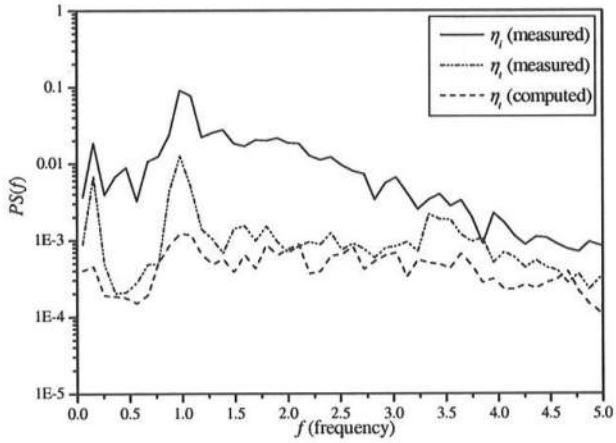

(f) Test 3.32

Figs. A.2(a)-(f) Power Spectra of Measured Incident Wave η_i as well as Measured and Computed Transmitted Wave η_t

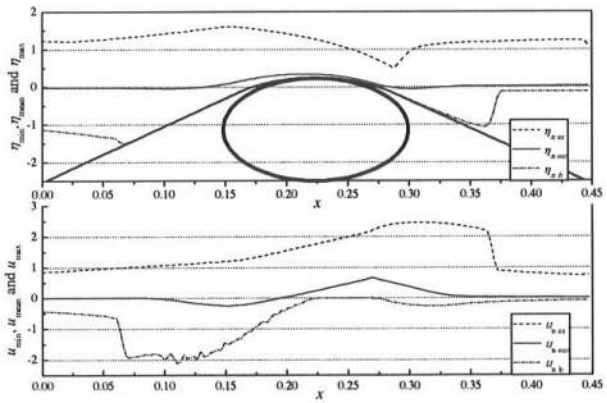

(a) Test 1.3

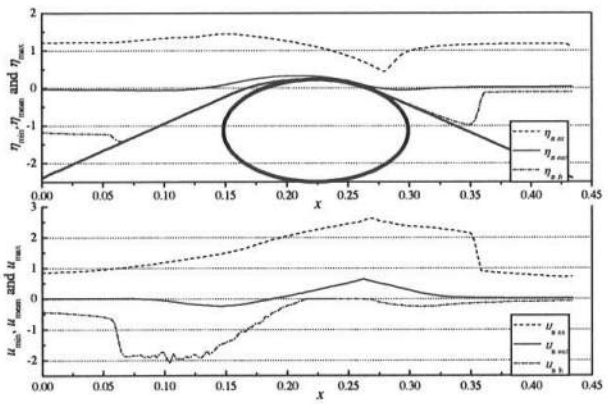

(b) Test 2.2

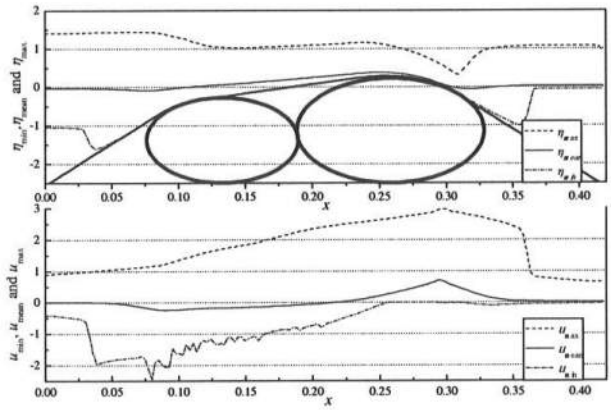

(c) Test 3.5

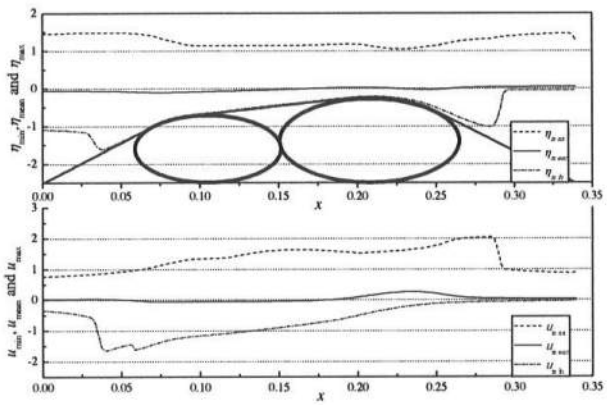

(d) Test 3.17

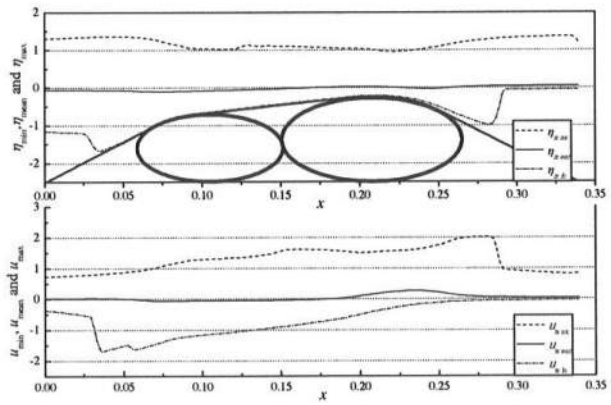

(e) Test 3.22

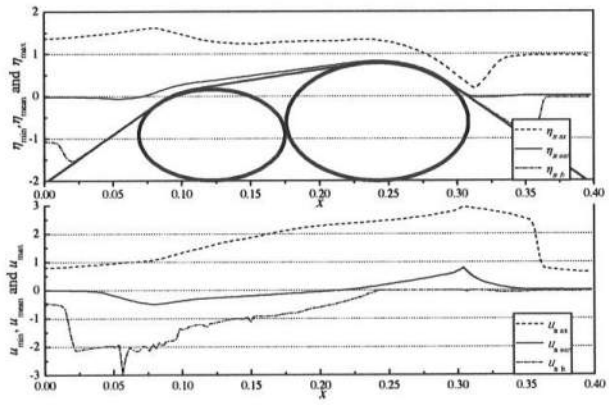

(f) Test 3.32

Figs. A.3(a)-(f) Computed Spatial Variations of Free Surface Elevation η and Depth-Averaged Velocity u

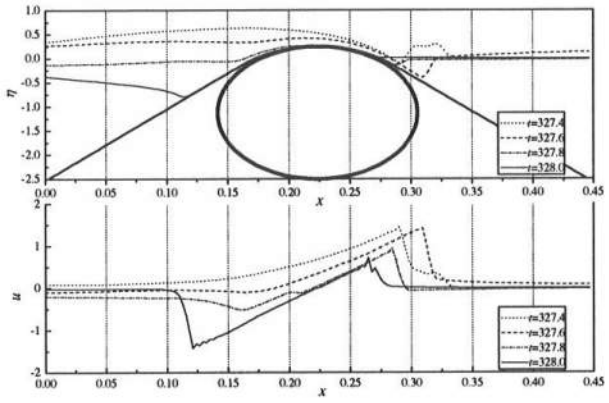

(a) Test 1.3

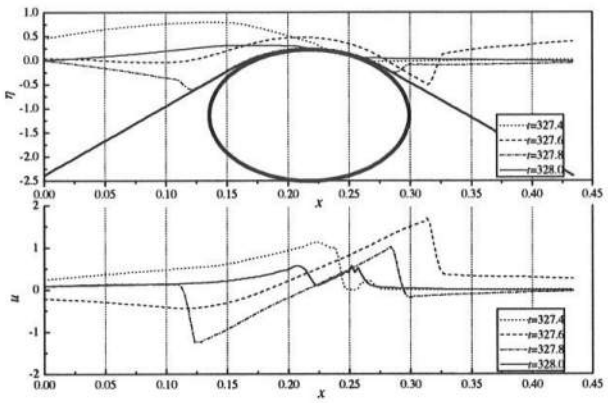

(b) Test 2.2

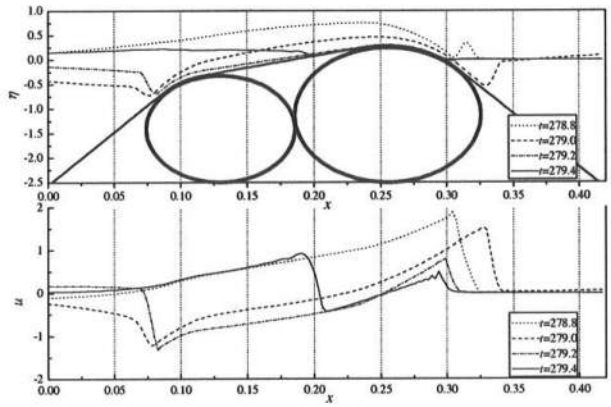

(c) Test 3.5

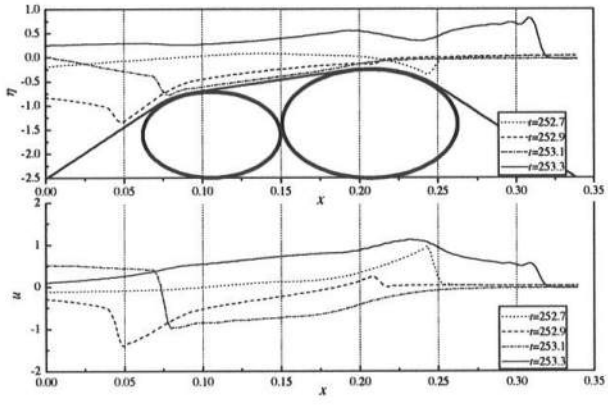

(d) Test 3.17

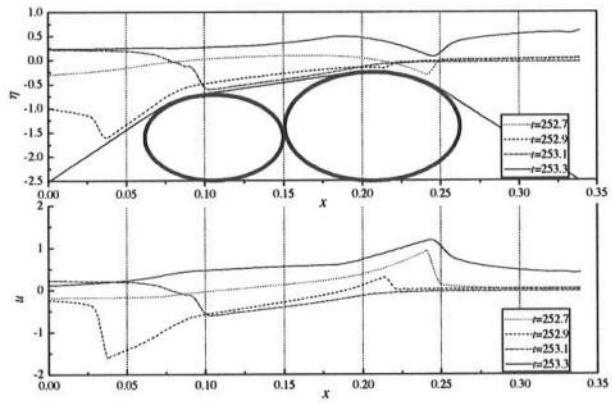

(e) Test 3.22

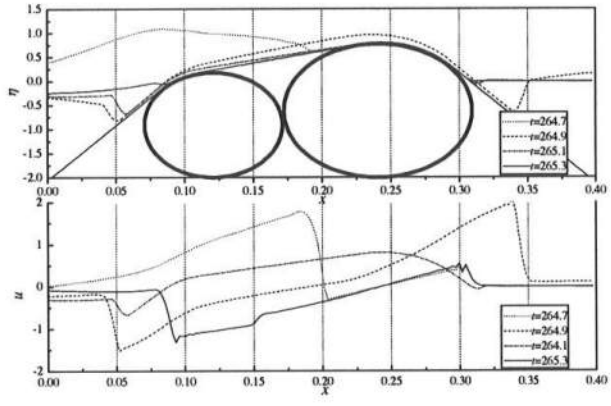

(f) Test 3.32

Figs. A.4(a)-(f) Spatial Variations of η and u at Specified Time Levels

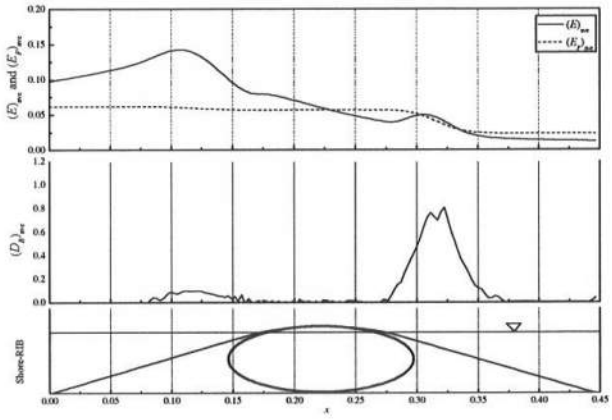

(a) Test 1.3

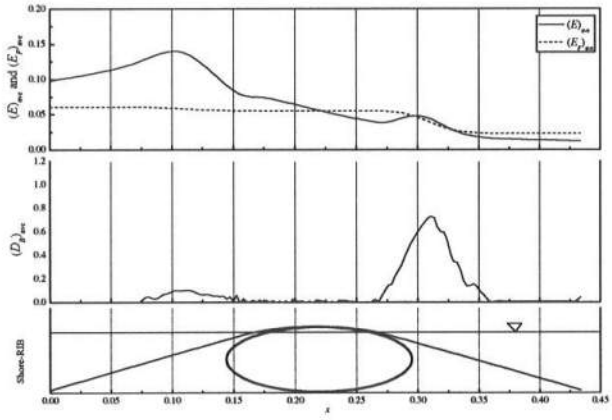

(b) Test 2.2

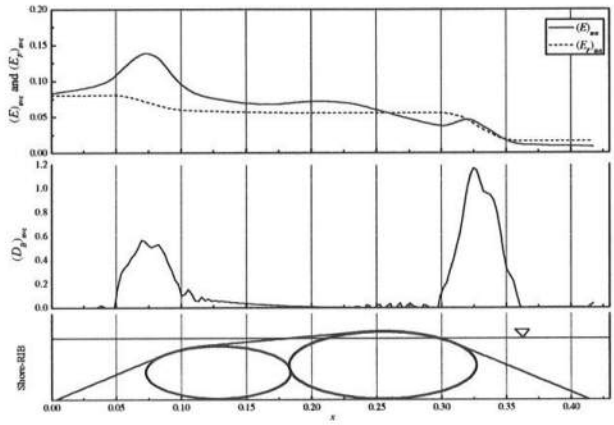

(c) Test 3.5

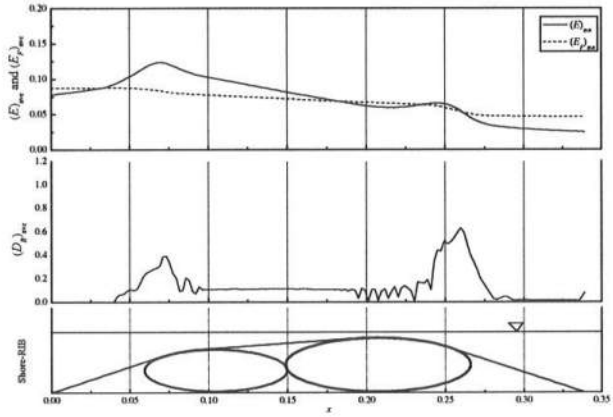

(d) Test 3.17

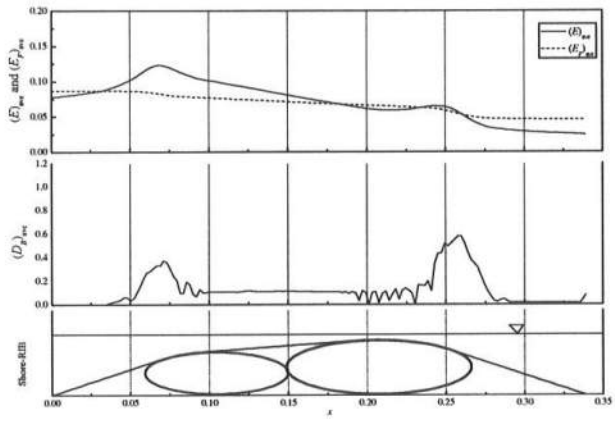

(e) Test 3.22

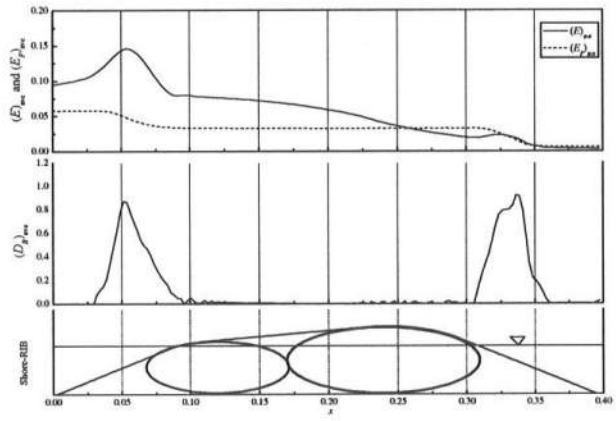

(f) Test 3.32

Figs. A.5(a)-(f) Spatial Variations of Time-Averaged Energy Quantities

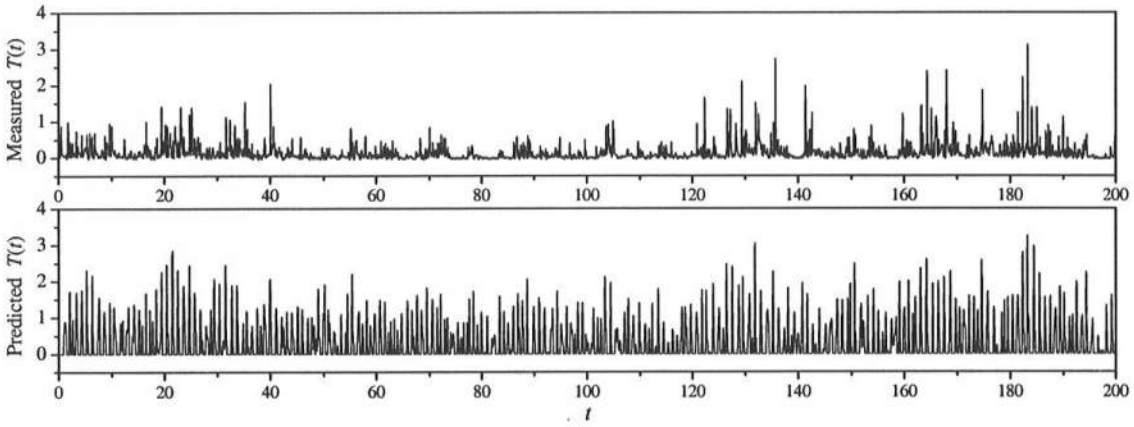

(a) Test 1.3

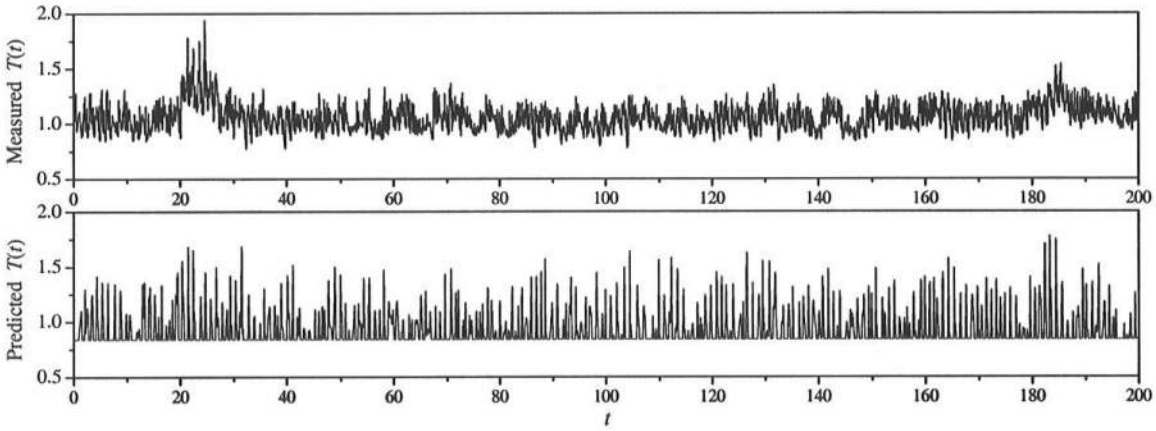

(b) Test 2.2

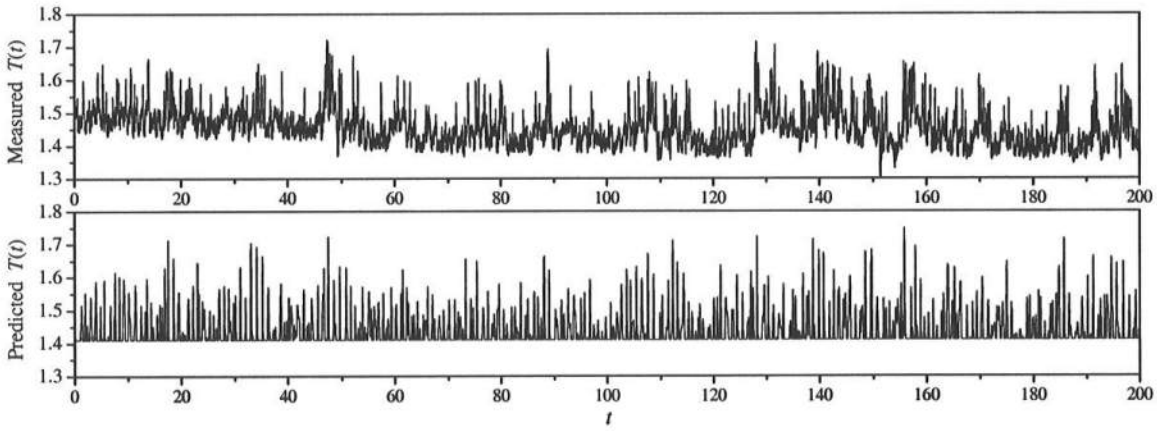

(c) Test 3.5

Figs. B.1(a)-(c) Temporal Variations of Measured and Predicted Tension $T(t)$

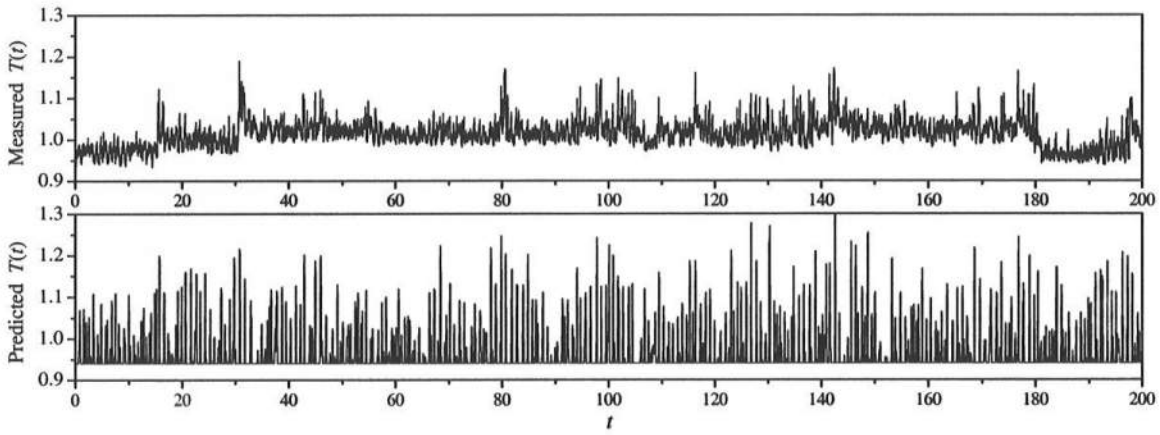

(d) Test 3.17

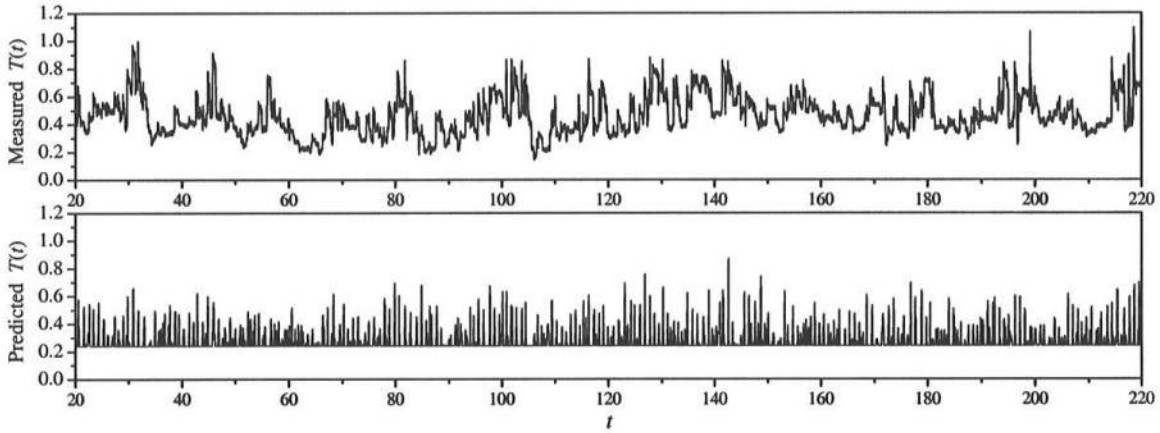

(e) Test 3.22

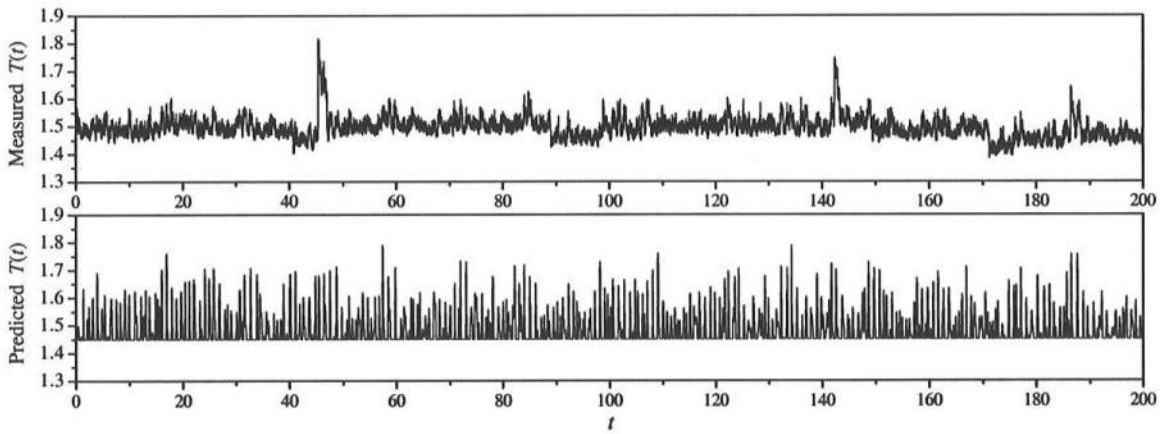

(f) Test 3.32

Figs. B.1(d)-(f) Temporal Variations of Measured and Predicted Tension $T(t)$

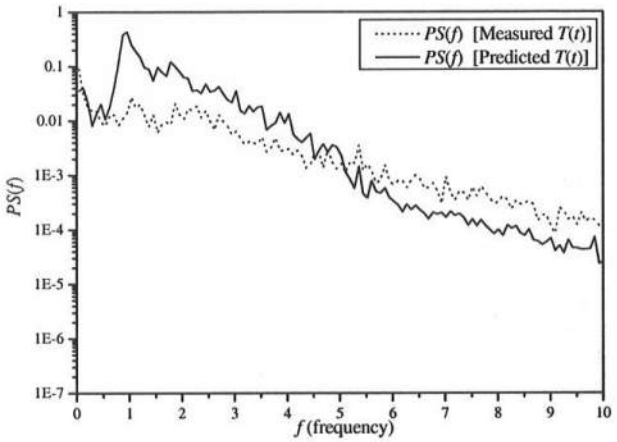

(a) Test 1.3

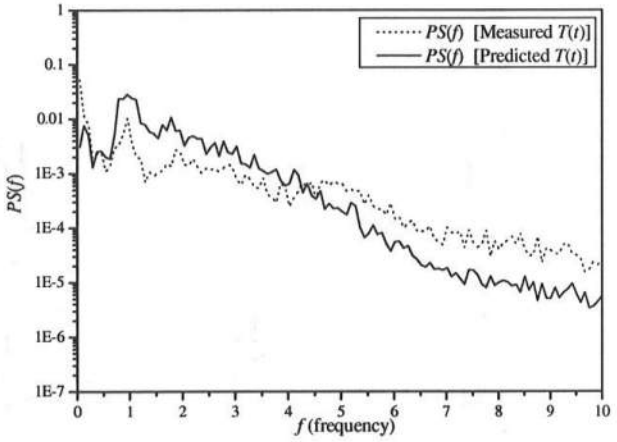

(b) Test 2.2

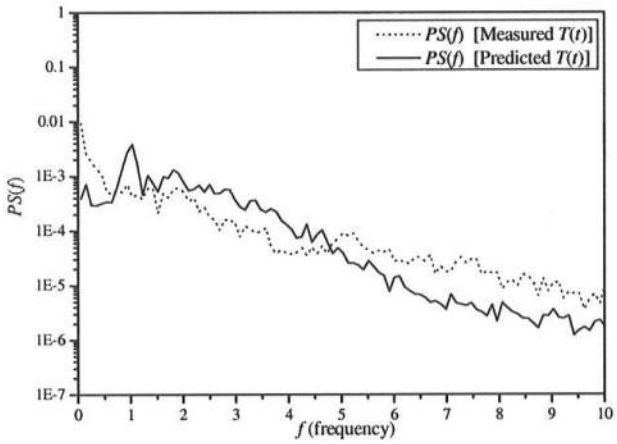

(c) Test 3.5

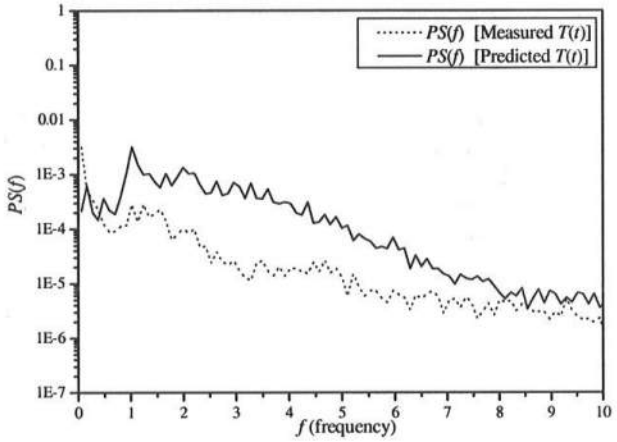

(d) Test 3.17

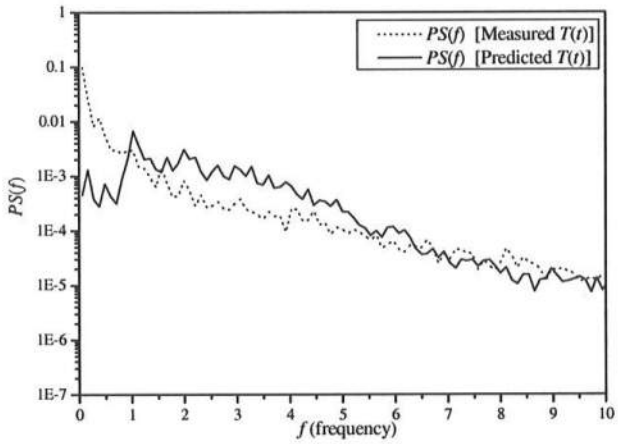

(e) Test 3.22

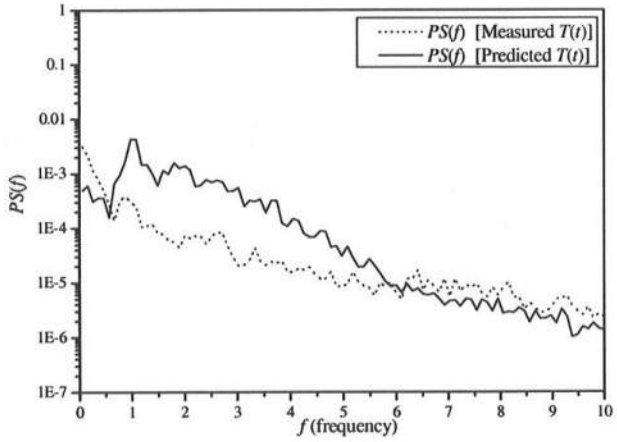

(f) Test 3.32

Figs. B.2(a)-(f) Power Spectra of Measured and Predicted Tension $T(t)$